A. B. Sturm, P. Visintin and D. J. Oehlers

Rational design approach for the instantaneous and time-dependent serviceability deflections and crack widths of FRC and UHPFRC continuous and simply supported beams

Journal of Structural Engineering, 2019; 145(11):04019138-1-04019138-18

A RATIONAL DESIGN APPROACH FOR THE INSTANTANEOUS AND TIME DEPENDENT SERVICEABILITY DEFLECTIONS AND CRACK WIDTHS OF FRC AND UHPFRC CONTINUOUS AND SIMPLY SUPPORTED BEAMS

[1]Sturm, A.B., [2]Visintin, P. and [3]Oehlers, D.J

Sturm, A.B., Visintin, P. and Oehlers, D.J., 2019. Rational Design Approach for the Instantaneous and Time-Dependent Serviceability Deflections and Crack Widths of FRC and UHPFRC Continuous and Simply Supported Beams. *Journal of Structural Engineering*, *145*(11), p.04019138.

ABSTRACT

Novel mechanics based closed form solutions for the long- and short-term serviceability deflections and crack widths of fibre reinforced concrete (FRC) and ultra-high performance fibre reinforced concrete (UHPFRC) beams are presented. These solutions incorporate the bond properties from bond tests directly and as such obviate the need for a constant bond stress simplification and consequently the need for member calibration as is commonly required in code approaches. The closed form solutions are validated on 12 simply supported and 4 continuous UHPFRC beams as well as 10 normal strength FRC beams with good correlation. A design example is also included for a UHPFRC T-beam demonstrating the application of the solutions.

INTRODUCTION

Excessive deflections and crack widths under service loads have a significant negative impact on the long-term functionality, aesthetics and durability of reinforced concrete structures (Gilbert & Ranzi 2010; Standards Australia 2014). The addition of discontinuous fibres to either normal strength concrete to create fibre reinforced concrete (FRC) or to high strength mortars to create ultra-high performance fibre reinforced concrete (UHPFRC) has the potential to reduce the deflections and crack widths by allowing the transfer of stresses across flexural cracks (Stang & Aare 1992; Schumacher 2006).

The design of FRC materials is complicated by the variety of metallic and non-metallic fibres of different shapes and sizes that are now commonly available. Further, these fibres can be used at varying volumes (Brandt 2008) and in concretes of widely varying mix design ranging from normal strength mixes with coarse aggregates (Schumacher 2006) to very high strength mixes without coarse aggregates (Graybeal 2006; Oesterlee 2010; Sobuz et al. 2016). Design is made even more complicated due to the option to blend fibres (Park et al. 2012; Banthia et al. 2014; Fantilli et al. 2018; Visintin et al. 2018a; Sturm et al. 2018a). Hence, to be able to efficiently characterise the service deflections and crack widths of members with these materials, generic analysis techniques are required which can be related directly to the results of basic material tests without the need for member calibration.

In this paper, it is shown how a rational design approach for predicting instantaneous and time dependent deflections of FRC and UHPFRC materials can be developed based on fundamental partial interaction mechanics. Significantly, the proposed expressions are not based on experimental calibration, but rather on the direct application of material properties which are easily obtainable from simple, low cost experiments.

In the following, a literature review of current serviceability analysis approaches is first presented. This is followed by a description of the segmental approach (Visintin & Oehlers 2017; Sturm et al. 2018a) upon which the design procedure is based. It is then shown how the segmental approach can be used as the basis for developing a simplified design approach for quantifying the instantaneous and time dependent deflections and crack widths of simply supported and continuous FRC and UHPFRC beams. The approach is then validated against

26 existing test results covering a range of material properties. Finally, in the supplementary material, a realistic worked example is presented to determine the serviceability behaviour of a continuous T-beam.

REVIEW OF EXISTING ANALYSIS AND DESIGN APPROACHES

Existing serviceability analysis and design approaches for UHPFRC and FRC members are largely based on modifications of traditional sectional moment-curvature analyses that are solved either numerically (Barros & Figueiras 1999) or analytically (Taheri et al. 2011; Mobasher et al. 2015). Approaches suggested by national codes of practice such as the fib Model Code 2010 (fib 2013) for normal strength FRC and the AFGC (AFGC 2013) for the design of UHPFRC are also moment-curvature based approaches. Approaches based on computing a flexural rigidity have been suggested by Amin et al. (2017) and AS3600-2018 (Standards Australia 2018). Approaches based on the rotation of a segment rather than the curvature of a cross section have also been suggested by Barros et al. (2015) and Visintin & Oehlers (2018), in their current form they are however more suited for numerical implementation.

As the focus of this paper is on design, the following review focuses on the critical points of analytical models as well as those proposed in the design standards rather than on more complex numerical models.

When considering the contribution of fibres post cracking, a number of existing approaches (Mobasher et al. 2015; Amin et al. 2017; Standards Australia 2018) assume a constant post cracking stress. Although leading to relatively simple analytical solutions, the limitation of this assumption is that it is known that the tensile stress resisted by fibres reduces with continued crack opening (Wille et al. 2014). Hence calibration is required to determine the most appropriate magnitude for the constant post cracking stress based on the expected crack width.

To improve the versatility of the solution, in this paper a piecewise linear stress crack width relationship is considered.

In the fib Model Code 2010 (fib 2013) and the AFGC recommendations (AFGC 2013). The tensile stress/crack width relationship is converted into a stress strain relationship by dividing by a characteristic length. In AFGC (2013) this is taken as 2/3 the depth of the section, while in fib (2013) the characteristic length is taken as a function of the crack spacing. The approach taken in the fib Model Code (2010) is followed in this paper as it considers the mechanical relationship between crack widths, crack spacings and deformation in the tensile zone of the beam.

When considering the impact of fibres on tension stiffening behaviour, existing approaches have been found either to not consider the effect of tension stiffening (Taheri et al. (2011), Mobasher et al. (2015), AS3600-2018 (Standards Australia 2018)), or to consider tension stiffening as a constant decrease in curvature (Amin et al. 2017). In Amin et al. (2017) the magnitude of tension stiffening is derived based on the assumption of a constant bond stress between the reinforcement and surrounding concrete. Experimentally it is observed that the bond stress increases with slip (Harajli et al. 1995) and hence this assumption requires calibration based on the expected slip of the reinforcing bar.

In AFGC (2013), tension stiffening is allowed for by multiplying the curvature by the ratio of the reinforcement strain at the crack and the mean reinforcement strain along the tension chord. The mean reinforcement strain is calculated using the expression of the mean difference in strains between the concrete and the reinforcement in the crack width expression and includes a bond factor which needs to be calibrated for new combinations of materials.

A number of other tension stiffening models are available in the literature which could be used in conjunction with flexural models to predict the tension stiffening effect. For example the widely applied bond factor approach of Bischoff (2003) has been extended to FRC, but as with the model proposed by AFGC (2013) calibration is required for new materials. Models based on the assumption of constant bond stress have also been suggested by Yuguang et al. (2009).

In contrast to these design oriented models, Lee et al. (2012) has suggested a fully non-linear tension stiffening model in which a non-linear bond slip relationship is considered between the reinforcement and the concrete as well as the pull out of each individual fibre. Although this model fully captures the mechanics of tension stiffening, in the context of the work proposed here it is considered too complex for application in a closed form analytical solution.

Hence, in this paper the tension stiffening model proposed by Sturm et al. (2018b) will be adopted to compute crack spacing and the response of the tensile reinforcement as it avoids the need for calibration by considering a realistic non-constant tensile stress/crack width response of the tensile concrete and bond stress-slip behaviour of the interface, while still resulting in closed-form solutions. In Sturm et al. (2018b), this model has been validated against 18 tension stiffening specimens ranging from normal strength to ultra-high performance FRC. The model demonstrated good fit to both the experimentally observed load-deflection and load-crack width behaviour. This model also allows for the effect of shrinkage to be considered by offsetting the strains between the concrete and reinforcement. The age-adjusted effective modulus method can be used with this model to allow for the creep effects (Gilbert & Ranzi 2010).

Considering the methodologies adopted to determine the neutral axis depth, the majority of approaches suggest either an iterative approach or require the solution of a higher order higher-order polynomial (fib 2013; AFGC 2013; Amin et al. 2017; Standards Australia 2018) which can be done numerically. Alternatively, Taheri et al. (2011) and Mobasher et al. (2015) do not require iteration to solve for the neutral axis depth but the expressions presented are complex.

To apply the solution technique of Taheri et al. (2011) the moment and curvature need to be evaluated over a range of tensile strains to obtain a smooth curve, and hence the approach is not suited to design by hand calculation. Mobasher et al. (2015) does provide a simplified bilinear moment curvature relationship defined using the moment and curvature at yield and then at ultimate. However, this is seen to be more suitable for analysis at the ultimate limit state, because assuming that the flexural rigidity at serviceability is given by the secant stiffness through the yield point appears to be overly conservative. Hence in this paper the moment and curvature will be solved for in terms of the bottom fibre strain removing the need to iterate for the neutral axis depth. Also to remove the need to evaluate the moment and curvature for a large number of these points a simplified bilinear moment-curvature relationship is developed.

In terms of crack widths, fib (2013), AFGC (2013) and AS3600-2018 (Standards Australia 2018) all provide relationships in terms of a crack spacing multiplied by a mean difference in strains between the concrete and the reinforcement. However, all the expressions are dependent on the definition of semi-empirical factors. Amin & Gilbert (2018) have also suggested an approach for finding the crack width based on the tension stiffening model in Amin et al. (2017) which is based on the assumption of a constant bond. Other approaches have been suggested by Barros et al. (2018), Fantilli & Chiaia (2018) and Visintin & Oehlers (2018) however these approaches are not suitable for hand calculations. In this paper a crack width model is proposed that is based on the tension stiffening model in Sturm et al. (2018b) which uses realistic non-constant bond-slip and tensile stress/crack width relationships.

Another important factor for the deflection and cracking behaviour is the influence of time effects. In fib (2013) and AFGC (2013) shrinkage is allowed for by evaluating a shrinkage curvature and creep is considered using an age adjusted effective modulus. In AS600-2018 (Standards Australia 2018) time effects are allowed for by multiplying by a factor which is a function of the quantity of compressive reinforcement. In this paper shrinkage is allowed for directly by considering an offset in strains between the reinforcement and the concrete and the effect of creep is allowed for using an age-effected age adjusted modulus (Gilbert & Ranzi 2010).

FRC and UHPFRC COMPONENTS OF RC BEAM

Having reviewed existing approaches and identified the desired features for the new approach, consider the response of the components that comprise the RC beam in Fig. 1(a).

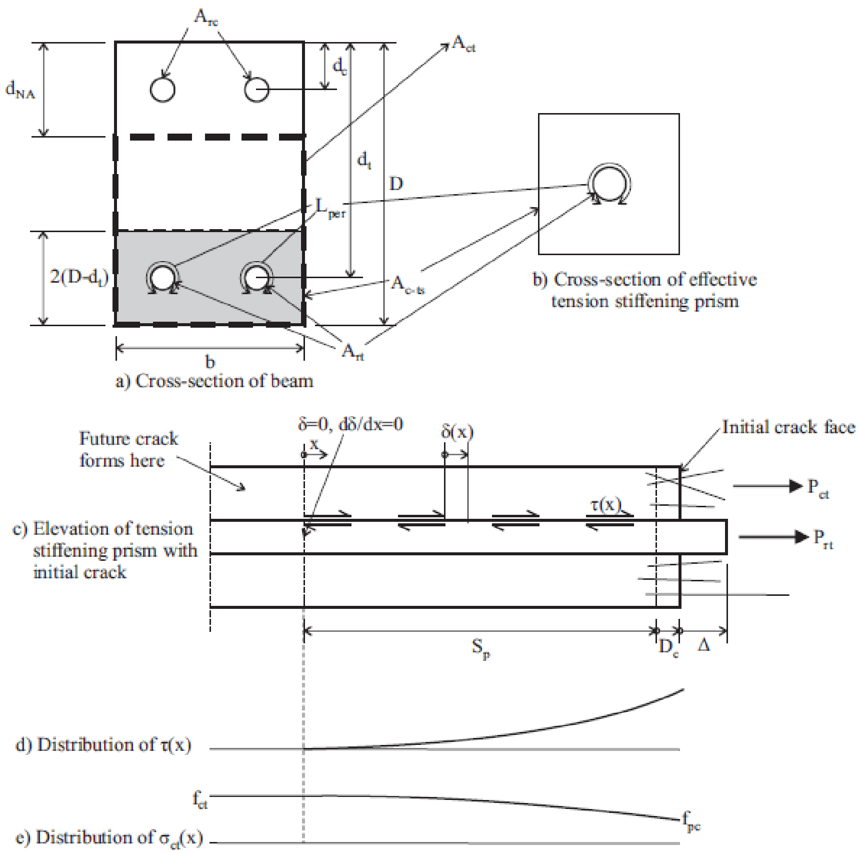

Fig. 1. Tension stiffening prism with an initial crack

Concrete in Tension

Wille et al. (2014) have suggested that the tensile response of UHPFRC can be divided into: (i) a strain based ‘linear elastic’ portion in the stress/strain relationship in Fig. 2(a); (ii) a strain based ‘strain hardening’ portion; and (iii) a crack opening based ‘softening’ portion in the stress/crack-width relationship in Fig. 2(b). During the first linear elastic phase in Fig. 2(a), the concrete is uncracked. During the strain hardening phase, microcracks are distributed throughout the volume. Finally, during the softening phase in Fig. 2(b), the deformation localises at a singular macrocrack.

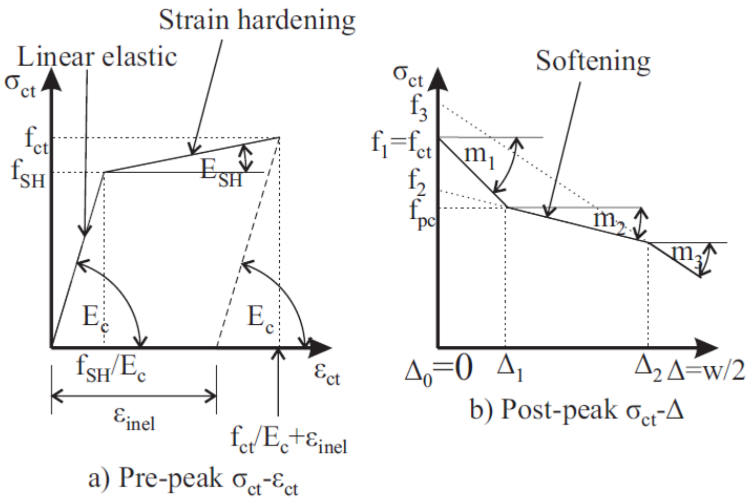

Fig. 2. Tension stress response of FRC

The stress in the concrete σ_{ct} in Fig. 2 can be represented analytically as a piecewise linear function of the strain ε_{ct} and half crack width Δ as:

$$\sigma_{ct} = E_c \varepsilon_{ct}; \varepsilon_{ct} \leq \frac{f_{SH}}{E_c} \quad (1a)$$

$$\sigma_{ct} = f_{SH} + E_{SH}\left(\varepsilon_{ct} - \frac{f_{SH}}{E_c}\right); \frac{f_{SH}}{E_c} < \varepsilon_{ct} < \frac{f_{ct}}{E_c} + \varepsilon_{inel} \quad (1b)$$

$$\sigma_{ct} = f_i - m_i \Delta; \Delta_{i-1} < \Delta < \Delta_i \; for \; i = 1, \ldots, n \quad (1c)$$

where in Fig. 2(a), E_c is the elastic modulus of the concrete, f_{SH} is the stress to cause microcracks, E_{SH} is the hardening modulus, f_{ct} is the tensile strength and ε_{inel} is the permanent strain due to microcracking. In Fig. 2(b), the stress f_i, where the subscript *i* is an integer, is the intercept with the stress axis, m_i is the slope and Δ_i is the right hand limit of the i^{th} component of the stress/half-crack-width relationship. The parameters in Eq. (1) can be obtained by fitted to the tensile response obtained from either a direct tension test or via inverse analysis of a flexural prism test.

It is also worth noting here that the post macrocracking response given by Eq. (1c) is represented as a stress/crack width relationship, and this can be rewritten here in terms of the half crack width by dividing the abscissa by 2. This approach is taken for convenience as it will be shown in the following that analysis can be conducted on a segment of half the crack spacing due to the presence of symmetry.

Having defined the stress-deformation relationship of the tensile concrete in Eq. (1), the axial force in the tensile concrete can be determined by integration as follows

$$P_{ct} = \int_{d_{NA}}^{D-d_{NA}} \sigma_{ct} dA = \sigma_{ct-ave} A_{ct} \tag{2}$$

where, in Fig. 1(a) A_{ct} is the area of concrete in tension and in a rectangular member this is $b(D-d_{NA})$. Further, the average stress in the tensile concrete σ_{ct-ave} in Eq. (2) can be approximated as a function of the strain at the bottom fibre ε_D in Fig. 3 by simply dividing the area under the stress/strain curve by the strain at the bottom fibre ε_D.as follows:

$$\sigma_{ct-ave} \approx \frac{\int_0^{\varepsilon_D} \sigma_{ct} d\varepsilon}{\varepsilon_D} \tag{3}$$

and which is exact if the area of tensile concrete has a constant width b.

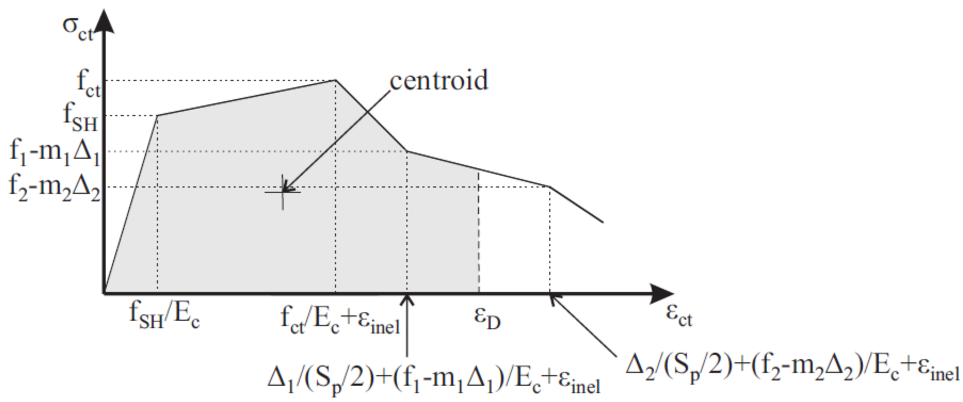

Fig. 3. Effective stress/strain relationship for the tensile concrete

To determine the average tensile stress for a section with macrocracks, the post-peak-stress/crack-width relationship needs to be converted to an equivalent stress/strain relationship. This is determined by considering that the elongation between two points is given by the strain in the material multiplied by the distance between the two points plus the opening of any fractures between the two points (Hillerborg 1978). Hence, the effective strain at a given depth is given by this elongation divided by the gauge length. The effective strain within the cracked region is therefore given by

$$\varepsilon_{ct} = \frac{\Delta}{\left(\frac{S_p}{2}\right)} + \frac{\sigma_{ct}}{E_c} + \varepsilon_{inel} \qquad (4)$$

where $\Delta/(S_p/2)$ is the contribution due to crack opening, σ_{ct}/E_c is the component due to the elastic deformation of the concrete between the cracks, and ε_{inel} is the component due to microcracking.

As a simplification to reduce the number of parameters that need to be defined, in this model it is assumed that the loading and unloading stiffnesses for the uncracked concrete are the same, even if the material is strain hardening. At this stage, this assumption is justified on two bases, firstly very little experimental work exists in which the unloading stiffness has been reported and secondly, Wille et al. (2014) has observed experimentally that for strain hardening FRCs the unloading stiffness is softer than the loading stiffness. Hence when determining the stress/crack width relationship by subtracting the elastic deformation from the total measured deformation between two points crossing a crack the assumption of an overly stiff unloading modulus results in a smaller predicted crack width, but as the predicted elastic deformation is greater the overall elongation is conserved.

Applying the above transformation to the stress/crack width relationship in Fig. 2(b) yields the stress/strain relationship in Fig. 3 where the lever arm of the tensile concrete l_{ct}, calculated with respect to the neutral axis is

$$l_{ct} = \frac{\int \sigma_{ct}(y-d_{NA})b\cdot dy}{\int_{d_{NA}}^{D-d_{NA}} \sigma_{ct} b\cdot dy} = \eta(D - d_{NA}) \tag{5}$$

In Eq. (5) η is the ratio of the distance of the centroid of the stress distribution from the neutral axis divided by the depth of the concrete in tension and is

$$\eta = \frac{\left(\frac{\int_0^{\varepsilon_D} \sigma_{ct}\, \varepsilon\, d\varepsilon}{\int_0^{\varepsilon_D} \sigma_{ct}\, d\varepsilon}\right)}{\varepsilon_D} = \frac{\int_0^{\varepsilon_D} \sigma_{ct}\, \varepsilon\, d\varepsilon}{\varepsilon_D^2 \sigma_{ct-ave}} \tag{6}$$

which is exact if the area of tension concrete has a constant width. That is, Eq. (6) is the centroid of the area under the stress/strain curve, illustrated in Fig. 3, divided by the strain at the bottom fibre ε_D.

Concrete in Compression

Under serviceability loading, the concrete acting in compression is assumed to be linear elastic as defined by the elastic modulus E_c. Hence for a rectangular compressive section in Fig. 1(a), the axial force in the compressive concrete is

$$P_{cc} = \int_0^{d_{NA}} \sigma_{cc}\, dA = \frac{1}{2} b d_{NA}^2 E_c \chi \tag{7}$$

and the location of the compressive concrete lever arm with respect to the neutral axis is 2/3 d_{NA}.

Reinforcement in Tension

Crack Spacing

The crack spacing, S_p is required to determine both the contribution of the tensile concrete and the width of the cracks. The analysis procedure for determining the crack spacing is based on the partial- interaction bond/slip analysis of an axially loaded prism and this general approach has been widely applied to similar problems in a variety of concretes in the past and with various bond stress slip relationships (Gupta & Maestrini 1990; Wu et al. 1991; Balazs 1993; Choi & Cheung 1996; Muhamad et al. 2012; Zhang et al. 2017; Sturm et al. 2018). Here the approach of Sturm et al. (2018) is taken as it has been explicitly formulated to accommodate both the influence of fibres as well as concrete creep and shrinkage with a non-constant bond stress slip relationship.

For analysis, the shaded region centred on the tensile reinforcement in Fig. 1(a) can be considered as an effective tension stiffening prism, as shown in Fig. 1(b). When an axial force P_{rt} is applied to the end of the reinforcing bar in the tension-stiffening prism in Fig. 1(c), the reinforcing bar slips Δ relative to the position of the crack face. This slip Δ also stresses the fibres spanning the crack width causing an axial force P_{ct} to be developed and the concrete to extent D_c from its original position. The shear stresses $\tau(x)$ in Fig. 1(d) develop along the reinforcing-bar/concrete interface, transferring the axial force into the surrounding concrete. These shear stresses are a function of the slip of the reinforcing bar $\delta(x)$ as given by the interface shear-stress/slip relationship in Fig. 4 and for which several material models for fibre reinforced and UHPFRC concrete are available (Harajli 2009; Yoo et al. 2015; Marchand et al. 2016; Sturm & Visintin 2018). The transfer of stresses along the reinforcing bar/concrete interface results in the distribution of stress in the concrete in Fig. 1(e) which is at a maximum at S_p as shown. From this distribution, it can be seen that there is a minimum distance S_p from the existing crack within which a new crack cannot form as the concrete stresses are below the maximum. The stress in the concrete varies from the post-cracking stress f_{pc} at the existing crack in Fig. 1(e) due to the fibres spanning the crack to the tensile strength f_{ct} at the position of the new crack.

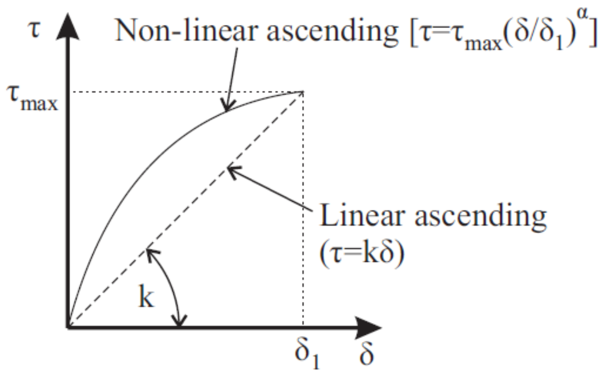

Fig. 4. Bond stress-slip relationship

By considering the definition of the slip δ(x) and force equilibrium for an infinitesimal segment of the tension stiffening prism, the following classical governing equation for the partial interaction behaviour along a bonded interface between two elastic materials as first developed by Volkersen (1938).

$$\frac{d^2\delta}{dx^2} = \beta\tau \tag{8}$$

where

$$\beta = L_{per}\left(\frac{1}{E_r A_{rt}} + \frac{1}{E_c A_{c-ts}}\right) \tag{9}$$

Considering the boundary condition that full interaction is reached at the new crack where the slip δ and the slip-strain dδ/dx is zero, and taking the non-linear ascending bond slip relationship in Fig. 4, the following expression for the crack spacing is derived (Sturm et al. 2018b)

$$S_p = \left[\frac{2^{\alpha}(1+\alpha)}{\lambda_2(1-\alpha)^{1+\alpha}}\right]^{\frac{1}{1+\alpha}}\left[\frac{f_{ct}-f_{pc}}{E_c}\left(\frac{E_c A_{c-ts}}{E_r A_{rt}}+1\right)\right]^{\frac{1-\alpha}{1+\alpha}} \quad (10)$$

where

$$\lambda_2 = \frac{\tau_{max} L_{per}}{\delta_1^{\alpha}}\left(\frac{1}{E_c A_{c-ts}}+\frac{1}{E_r A_{rt}}\right) \quad (11)$$

and τ_{max} is the maximum bond stress, δ_1 is the slip at the maximum bond stress and α is the power of the fitted power law all of which can be determined from the bond-slip relationship in Fig. 4. Equation (10) is also a function of the post-cracking stress in the tensile concrete, f_{pc} and this is defined as the stress corresponding to the first change of slope in the tensile stress/half crack width relationship and this is shown in Fig. 2(b).

The bond-slip relationship in Figure 4 is determined from pull out tests performed on reinforcing bars embedded in concrete prisms. Several recommendations exist for performing these simple material tests, for example RILEM has recommendations on how to perform this test for ordinary reinforced concrete (RILEM 1994) and several more recent studies have considered an extension to fibre reinforced concrete such that the suggested material properties are generally available (Harajli et al. 1995; Hota & Naaman 1997; Jungwirth & Muttoni 2004; Campione et al. 2005; Chao et al. 2009; Oesterlee 2010; Yoo et al. 2014, 2015; Marchand et al. 2016; Sturm & Visintin 2018). An inverse analysis can be performed to determine the local bond stress-slip relationship from the results of this test, however, as the bonded length is typically very short (2 bar diameters for UHPFRC, 5 bar diameters for normal strength FRC), it is usually sufficient to assume that the local bond stress-slip relationship is equivalent to the average bond stress versus slip obtained from these tests.

In the approach described above, the concrete tension stiffening prism has been taken to be symmetrical about each layer of the reinforcement as this ensures that a strain gradient is not introduced into the tension stiffening prism which cannot be accommodated for in this analysis. This approach has previously been applied in the numerical analysis of ordinary reinforced concrete (Visintin et al. 2013), fibre reinforced concrete (Visintin & Oehlers 2018) and beams combining prestressed and non-prestressed reinforcement by Knight et al. (2013; 2015). This is also the simplest approach to defining the area of the effective tension stiffening prism which is an advantage when analysing systems where different types and sizes of the reinforcement are considered. Alternatively, the fib Model Code 2010 (fib 2013) provides an expression for calculating the effective area which is not symmetrical, however this requires the use of an effective diameter of reinforcement when reinforcing bars of different sizes are combined or reinforcing bars and tendons are combined. It also requires the neutral axis depth to be known which is an issue for applying this approach as the crack spacing and the effective stiffness of the tensile reinforcement (see next section) are evaluated before the neutral axis depth is determined. The different choices in effective area of concrete results in negligible difference in the load-deflection response as shown in Fig. 5(a) and 5(c) using the properties of beams C1 and M1 from Table 1. The crack widths determined are also similar as shown in Fig. 5(b) and 5(d).

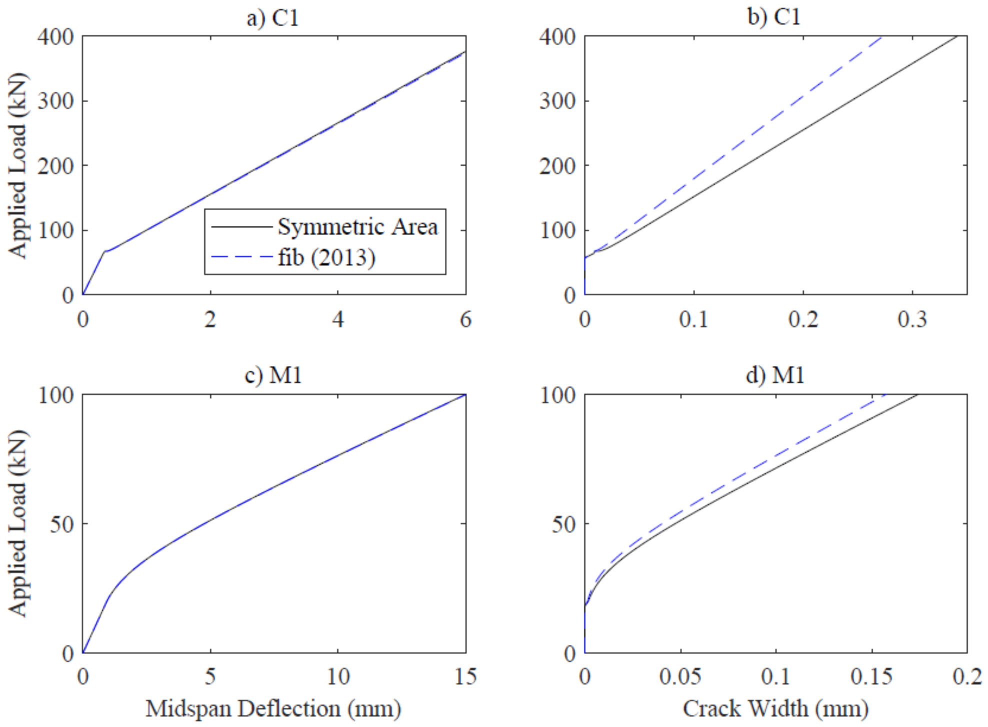

Fig. 5. Effect of the area of the effective tension stiffening prism

Axial force in the reinforcement prior to macrocracking

Before the formation of macrocracks, that is for strains less than $f_{ct}/E_c+\varepsilon_{inel}$, compatibility exists between the reinforcement and the surrounding concrete, therefore the force in the tension reinforcement in the beam in Fig. 1(a) is

$$P_{rt} = n_{FI} A_{rt} E_c \chi (d_t - d_{NA}) + P_{rt0} \tag{12}$$

where the compressive force due to the applied shrinkage strain, ε_{sh} is

$$P_{rt0} = -E_r A_{rt} \varepsilon_{sh} \tag{13}$$

n_{FI} is the modular ratio E_r/E_c and $\chi(d_t-d_{NA})$ is the strain at the level of the tensile reinforcement assuming a linear strain profile defined by a curvature, χ and neutral axis depth, d_{NA}. These are defined in the next section discussing the segmental method.

Axial force in the reinforcement after macrocracking

After the formation of macrocracks, that is for strains greater than $f_{ct}/E_c+\varepsilon_{inel}$, compatibility no longer exists between the concrete and the reinforcement. Hence an effective tension stiffening prism needs to be considered as shown in the cross-sections Figs. 1(a-b) and the elevation between two cracks in Fig. 6.

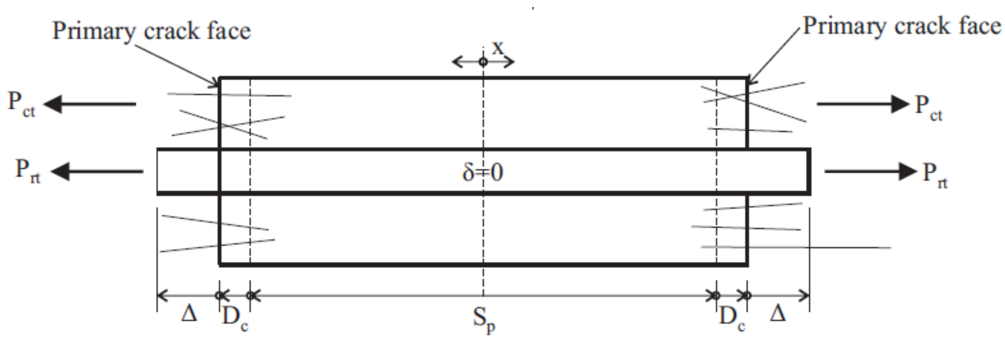

Fig. 6. Tension stiffening prism with two primary cracks

Considering the governing equation (Eq. (8)) and the new boundary conditions in Fig. 6, the following expression is obtained for the axial force in the reinforcing bar (Sturm et al; 2018a,b)

$$P_{rt} = \gamma n_{FI} A_{rt} E_c \chi (d_t - d_{NA}) + P_{rt0} \tag{14}$$

where $\chi(d_t\text{-}d_{NA})$ is the strain at the reinforcing bar as defined by a linear strain profile parameterised in terms of a curvature, χ and neutral axis depth, d_{NA}. These are defined in the next section discussing the segmental method. The force due to the applied shrinkage strain and fibres is given by

$$P_{rt0} = -E_r A_{rt} \varepsilon_{sh} - (\gamma - 1) E_r A_{rt} \left(\frac{f_i}{E_c} + \varepsilon_{inel}\right) \approx -E_r A_{rt} \varepsilon_{sh} \tag{15}$$

Further, in Eqns. (14) and (15) γ represents the increased stiffness due to tension stiffening (Sturm et al. 2018a) and is defined by

$$\gamma = \frac{\xi - n_f}{1 - n_f + \frac{\xi - 1}{\left(\frac{E_c A_{c-ts}}{E_r A_{rt}} + 1\right)}} \tag{16}$$

where the fibre contribution is given by

$$n_f = \frac{m_i}{E_c}\frac{S_p}{2} \tag{17}$$

and the contribution due to the bond is

$$\xi = \frac{\lambda_1 \frac{S_p}{2}}{\tanh\left(\lambda_1 \frac{S_p}{2}\right)} \tag{18}$$

where

$$\lambda_1 = \sqrt{kL_{per}\left(\frac{1}{E_r A_{rt}} + \frac{1}{E_c A_{c-ts}}\right)} \tag{19}$$

In Eq. (19) k is defined as the effective linear bond stiffness in Fig. 4 and Eqs. (15) and (16) are functions of f_i and m_i of which there are several possible values. The correct magnitude of Δ can be determined by checking that the slip at the reinforcing bar, is less than Δ_i and greater than Δ_{i-1} for the given load P_{rt}. In order to check this it is necessary to determine the slip of the reinforcement from the crack face, based on the partial-interaction mechanics above, Sturm et al. (2018b) has defined the relationship between P_{rt} and Δ as

$$\Delta = \frac{\frac{P_{rt}}{E_r A_{rt}} + \varepsilon_{sh} - \left(\frac{f_i}{E_c} + \varepsilon_{inel}\right)}{\xi - n_f}\left(\frac{S_p}{2}\right) \tag{20}$$

Significantly, Eq. (14) is in the same form as the expression for the full interaction case in Eq. (12) except that the stiffness of the reinforcement has been increased by the tension stiffening parameter, γ and there is an additional term in P_{rt0} which is a function of the strain in the tensile concrete. This shows that it is possible to directly incorporate the rational basis of tension stiffening and cracking without significantly changing the form of traditional design expressions.

It is also of note that in Eq. (15) a simplification has been suggested based on the observation that the additional stiffness of the reinforcement due to tension stiffening is usually on the order of 10% and hence in the second term of Eq. (15) (γ-1) is approximately 0.1. Further, since the shrinkage strain and ($f_i/E_c+\varepsilon_{inel}$) are of similar order of magnitude, the first term of Eq. (15) is an order of magnitude larger than the second, and hence the second can be ignored without significant loss of accuracy.

Reinforcement in compression

The compression reinforcement in Fig. 1(a) is assumed to be linear elastic. Therefore, the axial force in the reinforcement is

$$P_{rc} = n_{FI} A_{rc} E_c \chi (d_c - d_{NA}) + P_{rc0} \tag{21}$$

where the additional force due to the shrinkage strain is given by

$$P_{rc0} = -E_r A_{rc} \varepsilon_{sh} \tag{22}$$

FRC AND UHPFRC SEGMENTAL ANALYSIS

Qualitative description

Having now defined the internal forces in each component of a fibre reinforced concrete member, let us now consider how they can be incorporated into a flexural analysis procedure.

To determine the moment-rotation behaviour of a beam, first consider the uncracked segment in Fig. 7(a), where due to symmetry, for analysis the deformation length is L_{def} set equal to the half crack spacing (for an uncracked segment, any segment length is valid as there is no localisation, it is however convenient to set it to the half crack spacing). The initial position of the end of the segment is shown as profile A-A. Over time, a shrinkage strain develops in the segment and if the reinforcement were unbonded, this shrinkage would result in a contraction to profile B-B. However, due to the bond between the concrete and the reinforcement this contraction induces compressive forces in the reinforcement and to maintain equilibrium, tensile forces in the concrete. This results in the deformation profile C-C at a rotation $\theta_{sh.}$ If an external moment is applied, the rotation θ increases, to achieve force and moment equilibrium, resulting in the deformation profile D-D.

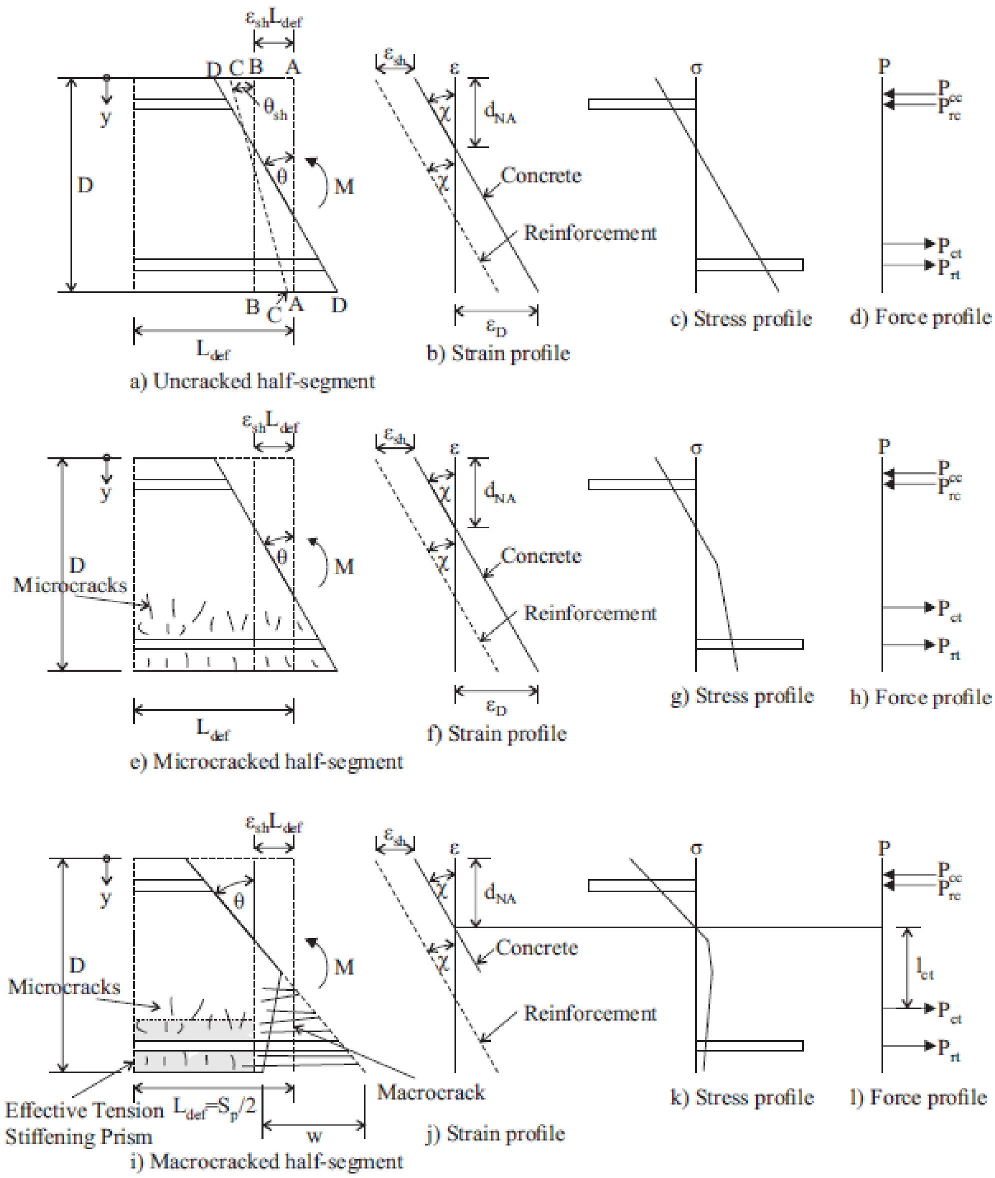

Fig. 7. Deformation, strain, stress and forces within a segment

The profile B-B in Fig. 7(a) represents the point at which the stress in the concrete is zero and profile A-A represents the point at which the stress in the reinforcement is zero. The result of this is that the effect of shrinkage can be modelled as an offset in concrete and reinforcement strains as illustrated Fig. 7(b) (Visintin et al. 2013; Sturm et al. 2018a); as such, the concrete strain ε_c is defined as the strains in the concrete that result in stress development. The effects of creep can also be allowed for by adjusting the elastic modulus of the concrete in accordance with the age adjusted effective modulus method (Gilbert & Ranzi 2010).

Dividing the deformation profile in Fig. 7(a) by the half segment length, L_{def}, results in the strain profile shown in Fig. 7(b), which represents the strain after the application of the shrinkage strain and external moment. Importantly a stain profile in Fig. 7(b) is defined for both the concrete and the reinforcement, and these are offset by the shrinkage strain. For further analysis d_{NA} will now be defined as the depth to the position where the strain is zero in the concrete.

Having now quantified the deformation and strain profiles, applying appropriate constitutive laws, the strain profile then results in the stress profile in Fig. 7(c), integration of which results in the force profile in Fig. 7(d). Using force and moment equilibrium, this system can then be solved to yield the relationship between the applied moment M and the rotation of the system θ and consequently from θ/L_{def} the moment and the curvature.

As the moment on the half-segment in Fig. 7(a) is increased, eventually the strain at the bottom fibre ε_D reaches the microcracking strain, f_{SH}/E_c. After this, the segment in Fig. 7(a) is replaced by Fig. 7(e). The presence of microcracks result in the hardening of the stress observed in Fig. 7(g) and when ε_D reaches the macrocracking strain, $f_{ct}/E_c+\varepsilon_{inel}$, macrocracks form as illustrated in Fig. 7(i). In this situation, the width of the macrocrack *w* is equal to the twice the difference between the deformation profile and the extension of the concrete in the tension stiffening prism given by Eq. 20. This also results in the softening in the tensile response illustrated in Fig. 7(k). At this stage, tension stiffening occurs increasing the effective stiffness of the tensile reinforcement. This is represented by multiplying the axial rigidity of the reinforcement by the tension stiffening parameter given by Eq. (16).

Hence by applying this moment/rotation approach, the moment/curvature and moment/crack-width relationship can be obtained and this allows us to assess the deflections and crack widths within the section.

Quantitative analysis

Having defined qualitatively the manner in which the segmental method can be applied using Fig. 7, and having previously established constitutive relations for both the crack spacing and the axial force/deformation relations for the various components of the beam, a procedure is now established for obtaining the moment/curvature and moment/crack-width relationships. As this approach is derived directly from the segmental analysis without modification, it will be referred to as the exact approach.

First a strain at the bottom fibre of the beam ε_D is imposed. The average stress in the tensile concrete $\sigma_{ct\text{-}ave}$ and the lever arm parameter η can now be evaluated from Eqs. (3) and (6) respectively and from Figs. 7(b), 7(f) and 7(j), the curvature is:

$$\chi = \frac{\varepsilon_D}{D-d_{NA}} \tag{23}$$

The neutral axis depth can be determined by considering force equilibrium and the expression for the curvature in Eq. (23). For a rectangular section and from Eqs. (2), (7), (14) and (21), the following is obtained

$$0 = \gamma n_{FI} A_{rt} E_c \chi (d_t - d_{NA}) + P_{rt0} + n_{FI} A_{rc} E_c \chi (d_c - d_{NA}) + P_{rc0} + \sigma_{ct-ave} b (D - d_{NA}) - \frac{1}{2} b d_{NA}^2 E_c \chi \tag{24}$$

Substituting Eq. (23) into Eq. (24) and rearranging gives the following quadratic equation for the neutral axis depth

$$0 = a_0 + a_1 d_{NA} + a_2 d_{NA}^2 \tag{25}$$

where

$$a_0 = E_c\varepsilon_D(\gamma n_{FI}A_{rt}d_t + n_{FI}A_{rc}d_c) + (P_{rt0} + P_{rc0})D + \sigma_{ct-ave}bD^2 \qquad (26a)$$

$$a_1 = E_c\varepsilon_D(\gamma n_{FI}A_{rt} + n_{FI}A_{rc}) - (P_{rt0} + P_{rc0}) - 2\sigma_{ct-ave}bD \qquad (26b)$$

$$a_2 = \sigma_{ct-ave}b - \frac{1}{2}bE_c\varepsilon_D \qquad (26c)$$

Having solved for the neutral axis depth in Eq. (26), the curvature can be evaluated using Eq. (23) and the forces in the concrete and reinforcement can then be evaluated using Eqs. (2), (7), (14) and (21). From this, the external moment M on the section can be determined. The crack width at a given depth can also be evaluated as the crack width w is equal to 2Δ, hence, rearranging Eq. (4) gives

$$w = S_p\left[\chi(y - d_{NA}) - \frac{\sigma_{ct}}{E_c} - \varepsilon_{inel}\right] \geq 0 \qquad (27)$$

Using this process, the moment/curvature and moment/crack-width relationships can be evaluated parametrically for a range of bottom strains ε_D. Note that Eq. (27) gives the maximum crack width of the section due to the assumptions made when deriving the crack spacing in Sturm et al. (2018b) which result in the definition of the minimum crack spacing. This is deemed sufficient as the maximum crack width is the parameter of interest in design.

This approach is applicable to all three segment types shown in Figs. 7(a), 7(e) and 7(i). For an uncracked segment: ($\varepsilon_D<f_{SH}/E_c$) , $\gamma=1$, $\sigma_{ct-ave}=(1/2)E_c\varepsilon_D$ and $\eta=2/3$ and in this case, w=0 for any value of y and a_2 is equal to zero from Eq. (26c). The neutral axis depth d_{NA} can then be evaluated as $-a_0/a_1$.

For a microcracked segment ($f_{SH}/E_c \leq \varepsilon_D < f_{ct}/E_c+\varepsilon_{inel}$), $\gamma=1$ while σ_{ct-ave} and η are given by the stress/strain relationship in Fig. 3 and the crack width, *w* is still taken as zero. The moments to cause micro- and macrocracking can be evaluated by substituting in the appropriate strains at the bottom fibre ε_D. For determining the moment at microcracking, a bottom strain of f_{SH}/E_c is applied while for determining the moment at macrocracking $f_{ct}/E_c+\varepsilon_{inel}$. For a segment with macrocracks ($\varepsilon_D>f_{ct}/E_c+\varepsilon_{inel}$), γ is calculated by Eq. (16) and $\sigma_{ct\text{-}ave}$ and η are given by the stress/strain relationship in Fig. 3.

SIMPLIFIED FRC AND UHPFRC SEGMENTAL ANALYSIS

The above approach is not ideal for hand calculations as it requires the evaluation of the moment, curvature and crack width over a range of bottom strains ε_D to obtain a smooth curve. To simplify this problem, the continuous moment/curvature relationship in Fig. 8(a) is replaced by a bilinear approximation.

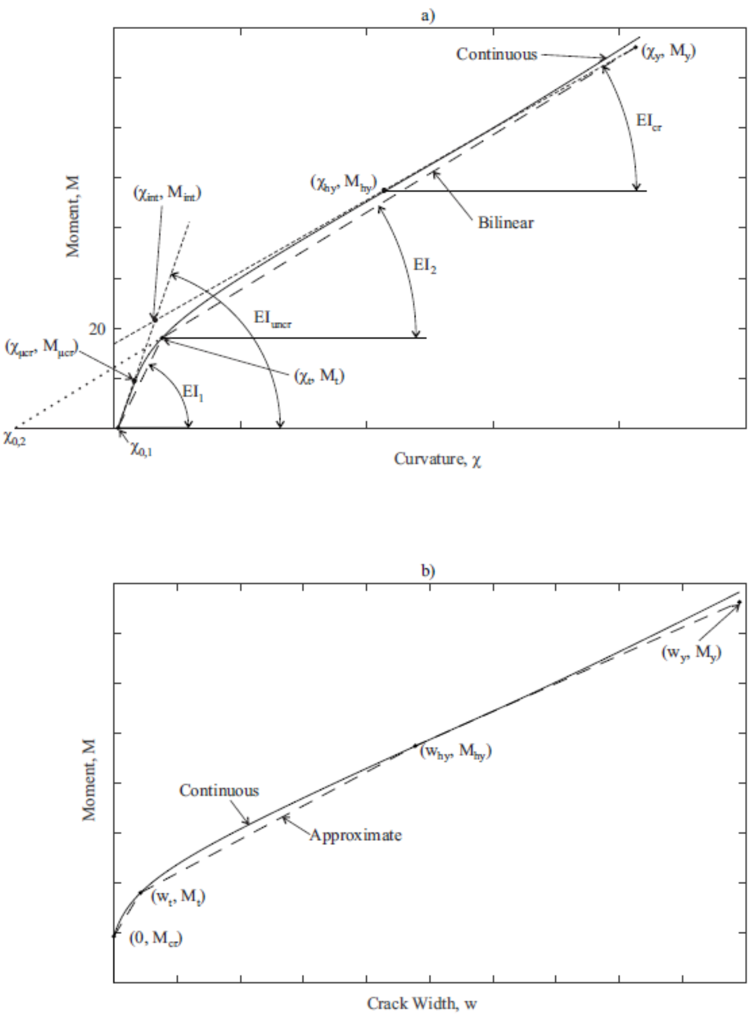

Fig. 8. Simplified moment-curvature and moment-crack width relationships

The functional form of the bilinear curve is

$$\chi = \chi_{0,1} + \frac{M}{EI_1}; M < M_t \tag{28a}$$

$$\chi = \chi_{0,2} + \frac{M}{EI_2}; M_t < M < M_y \tag{28b}$$

where $\chi_{0,1}$ is the curvature at zero moment due to shrinkage. The slope of the first portion of the bilinear curve is

$$EI_1 = \frac{M_t}{\chi_{t-\chi_{0,1}}} \tag{29}$$

The slope of the second portion of the bilinear curve is

$$EI_2 = \frac{M_y - M_t}{\chi_y - \chi_t} \tag{30}$$

and the intersection of the second portion of the bilinear curve with the curvature axis is

$$\chi_{0,2} = \chi_t - \frac{M_t}{EI_2} \tag{31}$$

Curvature at zero moment $\chi_{0,1}$

In this section, the curvature at zero moment is derived for a rectangular section as in Fig. 1(a). When the concrete is uncracked (ε_D<f_{SH}/E_c), the axial force is given by integrating the stress σ_c

$$P_c = \int_0^D \sigma_c \, dA = bE_c\chi_{0,1} \int_0^D (y - d_{NA0})\, dy = bE_c\chi_{0,1} \left[\frac{y^2}{2} - d_{NA0}y\right]_0^D = bDE_c\chi_{0,1} \left(\frac{D}{2} - d_{NA0}\right) \tag{32}$$

In Eq. (32) the stress in the concrete is assumed to be linear elastic because the strain is less than f_{SH}/E_c. The stress is therefore taken to be the elastic modulus, E_c multiplied by the strain, which is itself expressed as a function of the curvature, $\chi_{0,1}$, neutral axis, d_{NA0} and distance from the top of the section, y, as $\chi_{0,1}(y-d_{NA0})$.

From the reinforcement response Eqs. (12) and (21), force equilibrium gives

$$0 = n_{FI}A_{rt}E_c\chi_{0,1}(d_t - d_{NA0}) - E_rA_{rt}\varepsilon_{sh} + n_{FI}A_{rc}E_c\chi_{0,1}(d_c - d_{NA0}) - E_rA_{rc}\varepsilon_{sh} + bDE_c\chi_{0,1}\left(\frac{D}{2} - d_{NA0}\right) \tag{33}$$

Which upon rearranging in terms of the curvature yields

$$\chi_{0,1} = \frac{E_r\varepsilon_{sh}(A_{rt}+A_{rc})}{E_c(S_0-A_0d_{NA0})} \tag{34}$$

where the first moment of the transformed area about the top fibre is

$$S_0 = n_{FI}A_{rt}d_t + n_{FI}A_{rc}d_c + \frac{1}{2}bD^2 \tag{35}$$

and the area of the transformed section is

$$A_0 = n_{FI}A_{rt} + n_{FI}A_{rc} + bD \tag{36}$$

The moment about the top fibre due to the concrete forces is

$$M_c = \int_0^D \sigma_c y\, dA = bE_c\chi_{0,1}\int_0^D (y - d_{NA0})y\, dA = bE_c\chi_{0,1}\left[\frac{y^3}{3} - d_{NA0}\frac{y^2}{2}\right]_0^D = bD^2E_c\chi_{0,1}\left(\frac{D}{3} - \frac{d_{NA0}}{2}\right) \tag{37}$$

Hence from moment equilibrium at the top fibre

$$0 = n_{FI}A_{rt}E_c\chi_{0,1}d_t(d_t - d_{NA0}) - E_rA_{rt}d_t\varepsilon_{sh} + n_{FI}A_{rc}E_c\chi_{0.1}d_c(d_c - d_{NA0}) - E_rA_{rc}d_c\varepsilon_{sh} + bD^2E_c\chi_{0,1}\left(\frac{D}{3} - \frac{d_{NA0}}{2}\right) \tag{38}$$

Rearranging (38) in terms of curvature gives

$$\chi_{0,1} = \frac{E_r\varepsilon_{sh}(A_{rt}d_t+A_{rc}d_c)}{E_c(I_0-S_0d_{NA}0)} \tag{39}$$

where the second moment of the transformed area about the top fibre is

$$I_0 = n_{FI}A_{rt}d_t^2 + n_{FI}A_{rc}d_c^2 + \frac{1}{3}bD^3 \tag{40}$$

Equating Eqs. (34) and (39) gives the neutral axis depth

$$e(S_0 - A_0 d_{NA0}) = I_0 - S_0 d_{NA0} \tag{41}$$

where

$$e = \frac{A_{rt}d_t + A_{rc}d_c}{A_{rt} + A_{rc}} \tag{42}$$

Such that

$$d_{NA0} = \frac{I_0 - eS_0}{S_0 - eA_0} \tag{43}$$

Having obtained the neutral axis depth using Eq. (43), the curvature at zero moment can be evaluated using Eq. (34) or (39).

Moment M_y and curvature χ_y at yield

The process for determining the moment at yield can be simplified as follows. The bottom strain ε_D in Fig. 3 is unknown at the onset of yield, and is required to determine the average stress in the tensile concrete, $\sigma_{ct\text{-}ave}$ and the lever arm of the tensile concrete, l_{ct}. As a simplification to allow closed form solutions for the yield moment, the portion of the effective tensile stress-strain curve up until microcracking ($\varepsilon_D < f_{SH}/E_c$) is ignored, and a linear relationship is proposed instead (shown in Fig. 9), where the intercept with the stress axis is given as f_1 and the slope is E_f. This simplification is justified as the yield strain, ε_y is typically an order of magnitude larger than the microcracking strain, f_{SH}/E_c, hence the height of the crack has almost reached the neutral axis. Therefore, from Eqs. (3) and (6):

$$\sigma_{ct-ave} = f_1 - \frac{1}{2}E_f\varepsilon_D = f_1 - \frac{1}{2}E_f\chi_y(D - d_{NA,y}) \tag{44}$$

and

$$\eta = \frac{\frac{1}{2}f_1 - \frac{1}{3}E_f\varepsilon_D}{\sigma_{ct-ave}} \tag{45}$$

Setting P_{rt} to the force at yield f_yA_{rt} and rearranging Eq. (14) gives the effective yield strain

$$\varepsilon_y = \frac{1}{\gamma}\left(\frac{f_y}{E_r} + \varepsilon_{sh}\right) \tag{46}$$

Consequently, the curvature at yield is

$$\chi_y = \frac{\varepsilon_y}{d_t - d_{NA-y}} \tag{47}$$

An expression can now be developed for the neutral axis depth. For a rectangular section: the force in the tensile reinforcement is f_yA_{rt} and the force in the compressive reinforcement is given by Eq. (21); the force in the compressive concrete is given by Eq. (7); and the force in the tensile concrete by Eq. (2). Hence, from force equilibrium

$$0 = f_yA_{rt} + n_{FI}A_{rc}E_c\chi_y\left(d_c - d_{NA-y}\right) + P_{rc0} + \left[f_1 - \frac{1}{2}E_f(D - d_{NA-y})\right]b\left(D - d_{NA-y}\right) - \frac{1}{2}bd_{NA-y}^2E_c\chi_y \tag{48}$$

Substituting Eq. (47) into Eq. (48) gives

$$0 = b_0 + b_1d_{NA-y} + b_2d_{NA-y}^2 \tag{49}$$

where

$$b_0 = \left(f_yA_{rt} + P_{rc0}\right)d_t + bf_iDd_t + \varepsilon_y\left(n_{FI}E_cA_{rc}d_c - \frac{1}{2}E_fbD^2\right) \tag{50a}$$

$$b_1 = -\left(f_yA_{rt} + P_{rc0}\right) - bf_i(D + d_t) - \varepsilon_y\left(n_{FI}E_cA_{rc} - E_fbD\right) \tag{50b}$$

$$b_2 = bf_i - \frac{1}{2}b\varepsilon_y(E_c + E_f) \tag{50c}$$

After the neutral axis depth is evaluated using Eq. (49), the curvature can be evaluated using Eq. (47) and then the moment can be determined after first evaluating the forces and lever arms, then calculating moments.

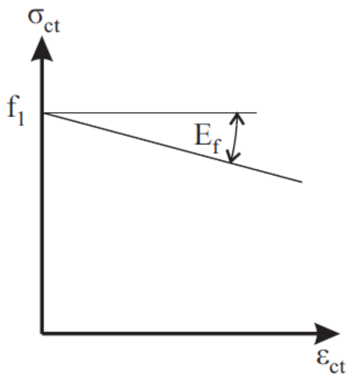

Fig. 9. Simplified tensile stress/strain curve

Moment M_t and Curvature χ_t at transition point

The first step to determine the transition point is to determine the uncracked flexural rigidity EI_{uncr} and the fully cracked flexural rigidity EI_{cr}. The uncracked flexural rigidity can be written as

$$EI_{uncr} = \frac{M_{\mu cr}}{\chi_{\mu cr} - \chi_{0,1}} \tag{51}$$

The moment and curvature at initiation of microcracking, $M_{\mu cr}$ and $\chi_{\mu cr}$ are determined by imposing a bottom strain ε_D of f_{SH}/E_c and following the procedure in the previous section. The fully cracked flexural rigidity is estimated by taking the secant stiffness through the yield point and the point where the bottom fibre strain is equal to 50% of the bottom fibre strain at yield, that is

$$EI_{cr} = \frac{M_y - M_{hy}}{\chi_y - \chi_{hy}} \tag{52}$$

where M_{hy} and χ_{hy} are the moment and the curvature, respectively, determined by setting the bottom strain, ε_D to $0.5\chi_y(D\text{-}d_{NA\text{-}y})$ and following the solution procedure in the previous section.

Having determined the uncracked and fully cracked flexural rigidities, the intersection between the two curves as illustrated in Fig. 8(a) can be found. Equating the curvature at the intersection given by the two curves, gives the curvature at the intersection

$$\chi_{int} = \chi_{0,1} + \frac{M_{int}}{EI_{uncr}} = \chi_y - \frac{M_y - M_{int}}{EI_{cr}} \tag{53}$$

Rearranging Eq. (53) also gives the moment at the intersection

$$M_{int} = \frac{\frac{M_y}{EI_{cr}} + \chi_{0,1} - \chi_y}{\frac{1}{EI_{cr}} - \frac{1}{EI_{\mu cr}}} \tag{54}$$

Hence the moment can be evaluated using Eq. (54) and then the curvature at the intersection from Eq. (53). The transition point is chosen to have the same bottom strain as for this hypothetical intersection point. To determine this, it is assumed that the bottom strain ε_D is proportional to χ. This is justified as ε_D is equal to χ $(D\text{-}d_{NA})$ and the variation in $(D\text{-}d_{NA})$ is significantly smaller than χ. The bottom tensile strain at transition is found by linearly interpolating between the strain at microcracking and $0.5\chi_y(d_t\text{-}d_{NA})$ as a function of the curvature which gives

$$\varepsilon_{D,t} = \frac{f_{SH}}{E_c} + \left[0.5\chi_y(D - d_{NA}) - \frac{f_{SH}}{E_c}\right]\frac{\chi_{int} - \chi_{\mu cr}}{\chi_{hy} - \chi_{\mu cr}} \tag{55}$$

Having determined the bottom strain, $\varepsilon_{D,t}$, the neutral axis depth can be evaluated with Eq. (25), the curvature with Eq. (23) and the axial forces in the reinforcement and concrete can with Eqs. (2), (7), (14) and (21). The moment, M_t can then be evaluated by multiplying these forces by their lever arms. The flexural rigidities of each portion of the curve can then be evaluated from Eqs. (29) and (30).

Estimating crack widths

As shown in Fig. 8(b), the crack width can be estimated by linearly interpolating between the crack widths evaluated at macrocracking ($\varepsilon_D = f_{ct}/E_c + \varepsilon_{inel}$), transition ($\varepsilon_{inel} = \varepsilon_{D,t}$) , half yield ($\varepsilon_D$ is 50% of the value at yield) and yield.

VALIDATION

Simply Supported Beams

In Fig. 10 the predicted load-deflection curves are compared to experimental results for simply supported UHPFRC beams and in Fig. 11 the predicted load-deflection curves are compared to experimental results for normal strength FRC beams. The details of each test specimen including the geometrical and material properties are summarised in Table 1.

For the UHPFRC beams reinforced with steel bars the bond properties were estimated using the material model detailed in Sturm & Visintin (2018), while for the GFRP reinforced beams tested by Yoo et al. (2016), the bond properties are estimated from the pullout tests contained in Yoo et al. (2015). In all cases, the tensile properties were obtained by fitting the tensile response model in Eq. (1) to the results from associated direct tension tests, however if direct tension test results were not available, inverse analysis of flexural prism tests to yield the stress/strain and stress/crack width behaviour could have been applied.

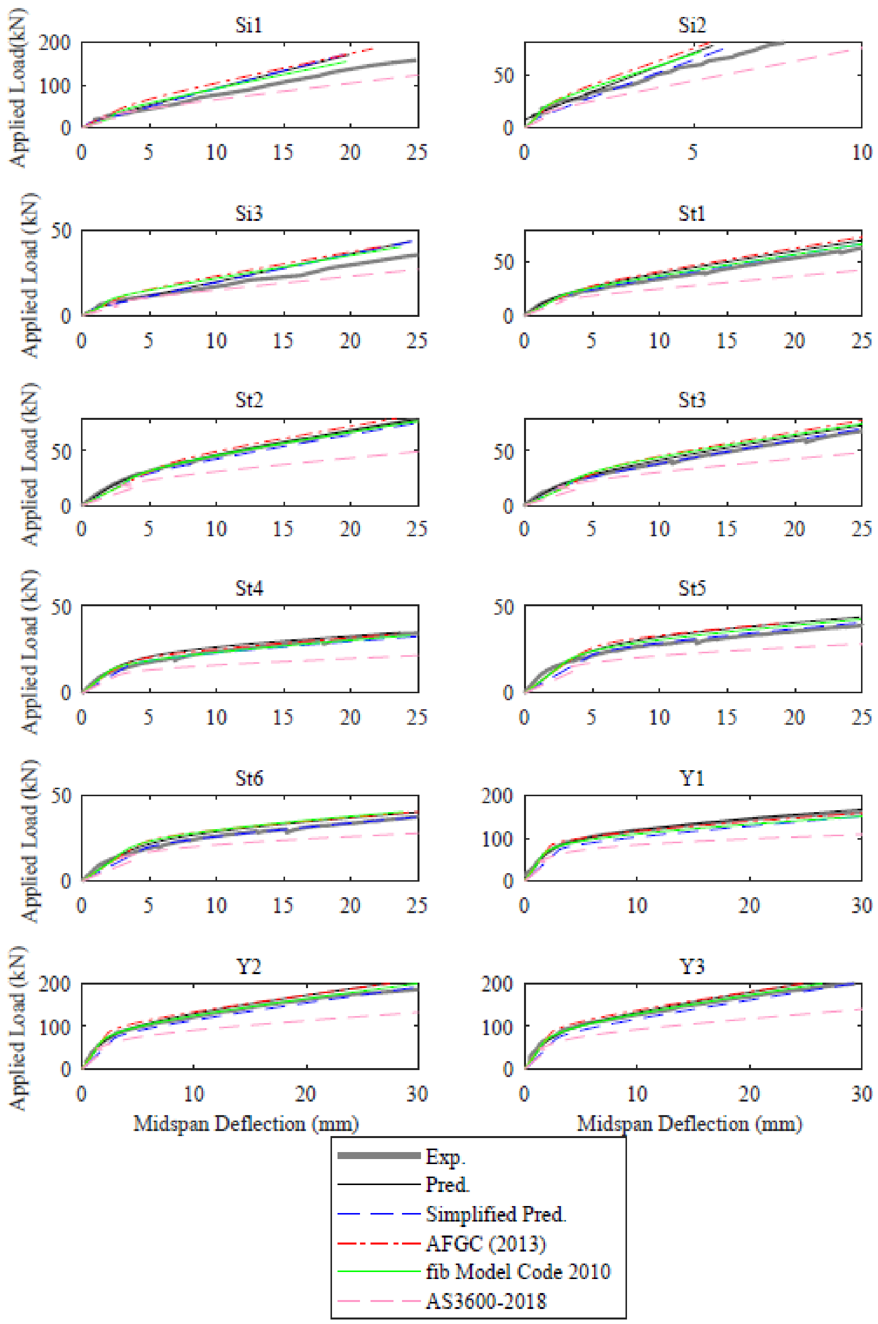

Fig. 10. Comparison of experimental to predicted load deflections for simply supported UHPFRC beams

For the normal strength FRC specimens the bond properties were estimated using the model of Harajli et al. (2009) and the tensile properties were back calculated from prism tests using the design expression in AS3600-2018 (Standards Australia 2018).

The shrinkage strains were determined directly from associated shrinkage tests, or if these were not available the shrinkage strain, ε_{sh} was assumed to be 500 $\mu\epsilon$ for UHPFRC beams. The shrinkage strain, ε_{sh} was assumed to be zero for the FRC beams as they were tested shortly after casting.

In the comparisons in Figs. 10 and 11, the mid-span deflection of the beam under four point loading with two different flexural rigidities can be derived using the proposed approach by considering the bending moment diagram under four-point loading. The curvature distribution can then be obtained from Eq. (28). Doubly integrating this curvature distribution while applying the boundary condition that the deflection is zero at the supports the following is obtained

$$\Delta_{mid} = \frac{F(L-a)}{96EI_2}[3L^2 - (L-a)^2] + \frac{1}{8}\chi_{0,2}L^2 - \frac{1}{6}Fx_1^3\left(\frac{1}{EI_2} - \frac{1}{EI_1}\right) - \frac{1}{2}\left(\chi_{0,2} - \chi_{0,1}\right)x_1^2 \quad (56)$$

where the boundary between the regions with different flexural rigidities is at

$$x_1 = \frac{2M_t}{F} \quad (57)$$

and in which F is the applied load (under four point loading it is the summation of the load applied at both load points), L is the span, and *a* is the spacing between the load points (this is zero for three point loading).

It can be seen in Figs. 10 and 11 that both the full (labelled Pred.) and approximate (Simplified Pred.) solutions give accurate predictions of the observed load-deflection behaviours (Exp.) for both conventional steel and glass fibre reinforced polymer reinforcement, as well as normal strength FRC and UHPFRC.

In Fig. 10 the results using the models in AFGC (2013), fib (2013) and AS3600-2018 (Standards Australia 2018) approaches are compared to the proposed approach. It is observed that the AFGC (2013) approach tended to underestimate the deflections, while the AS3600-

2018 (Standards Australia 2018) approach overestimated the deflection and fib (2013) approach gave similar results to the approach given in this paper.

In Fig. 11 the curves obtained using the approaches suggested by Amin et al. (2017), fib Model Code 2010 (fib 2013) and AS3600-2018 (Standards Australia 2018) are shown for comparison for the FRC test results. For the beams tested by Conforti et al. (2013) and Meda et al. (2012) it was found that all the approaches gave similar results for the load-deflection. For Ning et al. (2012) the approaches in this paper were accurate for N1 and N3 while underestimating the deflection for N2 and N4. Amin et al. (2017) underestimated the deflection for N2. fib Model Code 2010 overestimated the deflection for N1 and N3 while AS3600-2018 overestimated the deflection in every case.

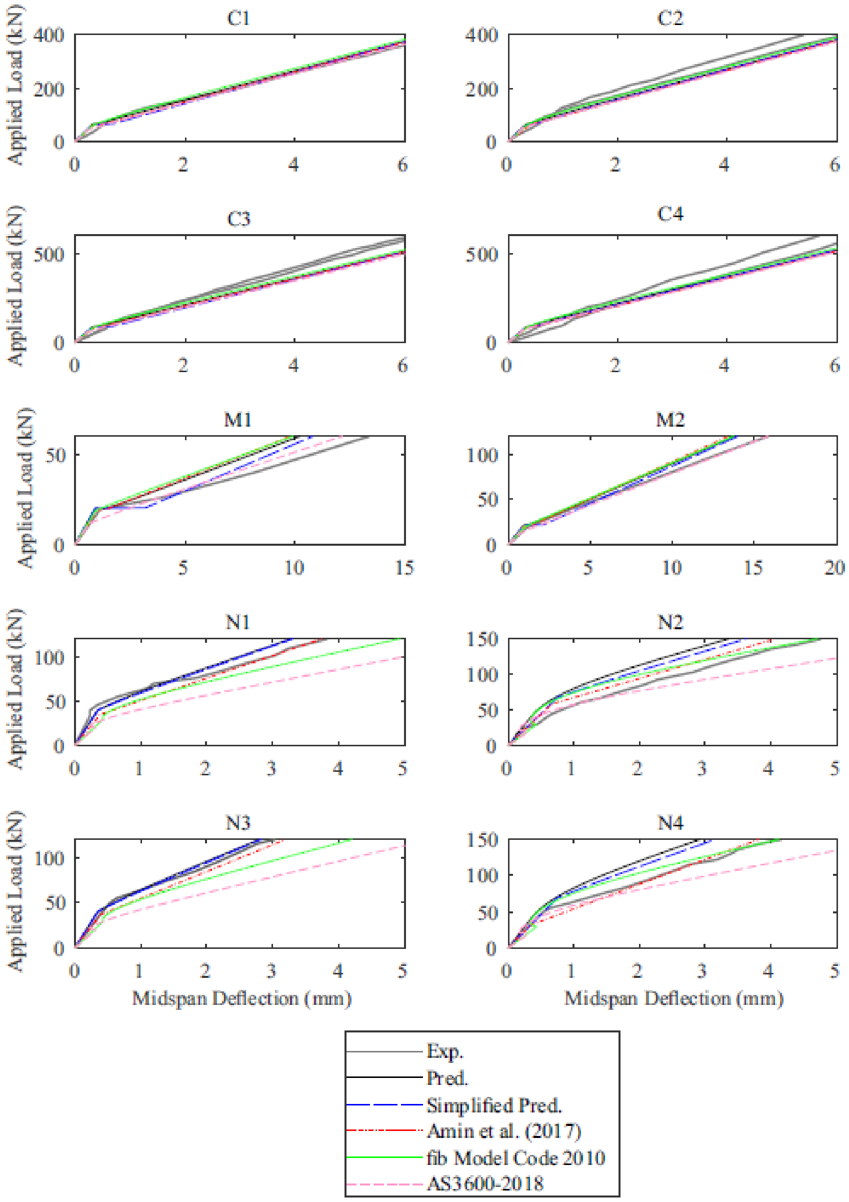

Fig. 11. Comparison of experimental to predicted load deflections for simply supported normal strength FRC beams

The maximum predicted crack widths from the expressions in this paper are compared against the experimental maximum crack widths for the beams tested by Sturm et al. (2018a) (St1-St6 in Fig. 12). The crack widths were measured at the depth of the reinforcement. The fit is deemed to be sufficient as the crack widths are characterised by significant random variation particularly in the presence of fibres as discussed in Deluce (2014). The AFGC (2013) expressions underestimates the crack widths in all cases while the fib (2013) and AS3600-2018 (Standards Australia 2018) expressions are close for the St1, St2 and St3 while they overestimate the crack widths for St4, St5 and St6.

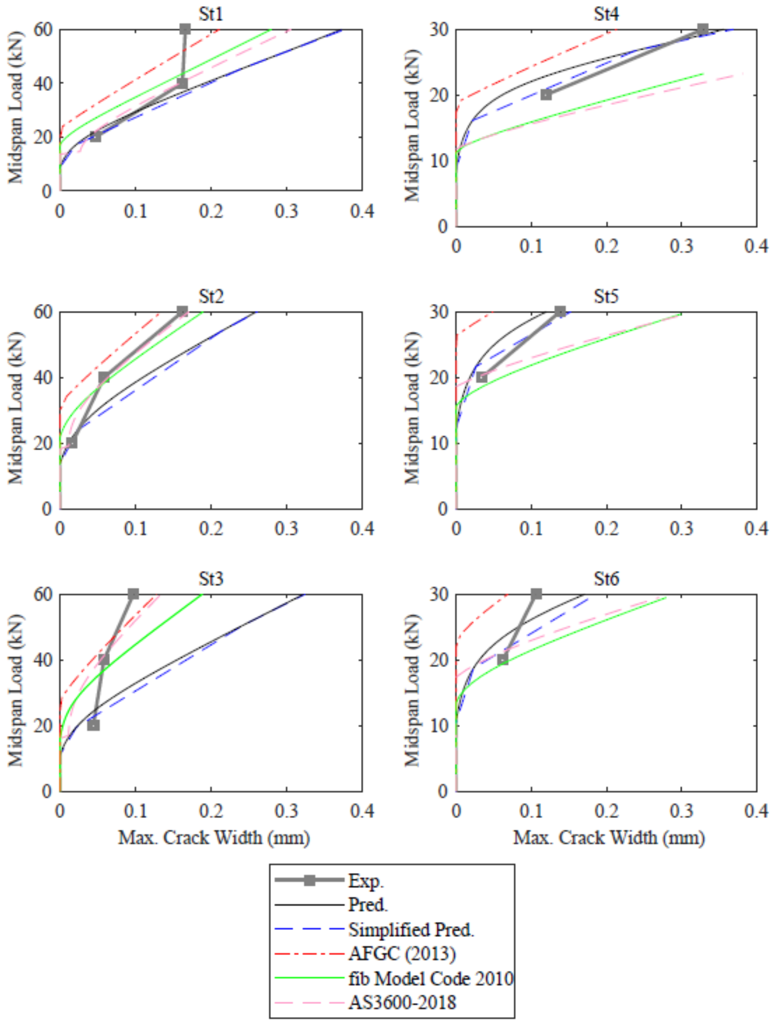

Fig. 12. Comparison of experimental to predicted crack widths for Sturm et al. (2018a)

Continuous Beams

The experimental and predicted results of two-span continuous UHPFRC beams tested by Visintin et al. (2018b) are shown in Fig. 13 and the properties of these beams is also summarised in Table 1.

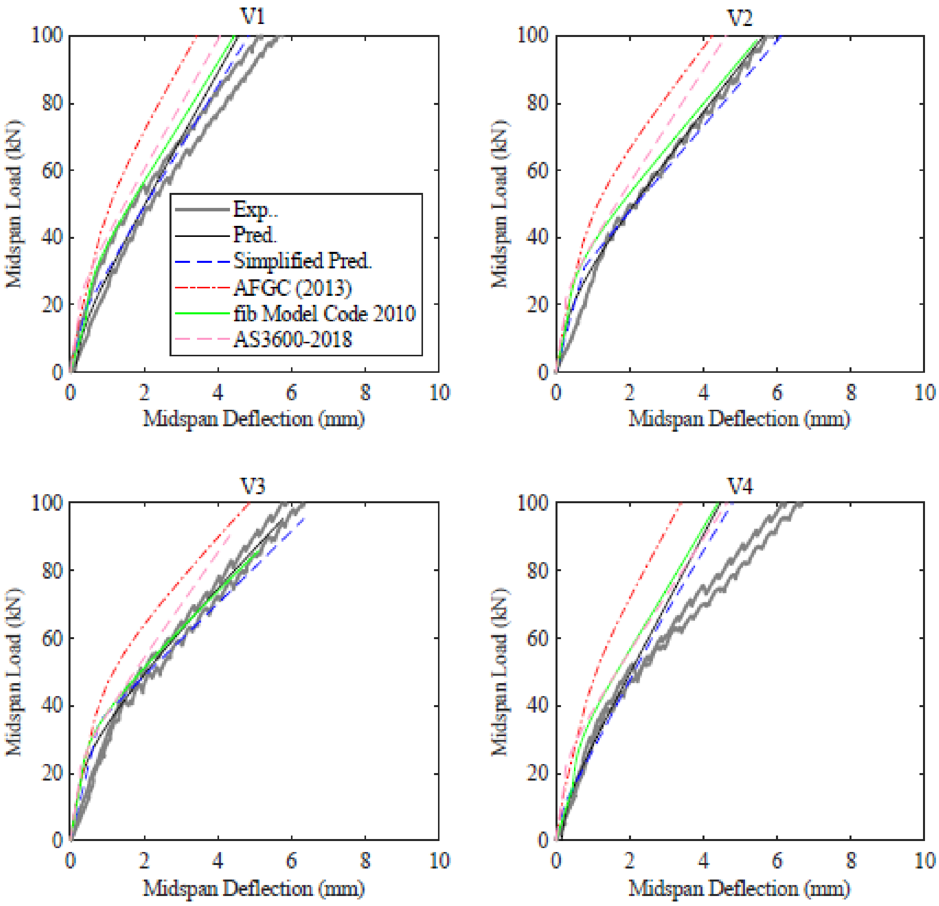

Fig. 13. Comparison of experimental to predicted load deflections for Visintin et al. (2018)

The deflection can be evaluated using any recognised structural mechanics approach using the flexural rigidities and curvature under zero moment presented in this paper. For the comparison with the experimental results, in this paper the deflection of the two span continuous beam loaded at the midpoints with different flexural rigidities in the hogging and sagging regions was obtained by doubly integrating the curvature along the beam to give

$$\Delta_{mid} = \frac{7FL^3}{768EI_{sag}} - \frac{1}{8}\chi_{0,sag}L^2 + \frac{Fx_1}{192}\left(\frac{1}{EI_{hog}} - \frac{1}{EI_{sag}}\right)\left(18L^2 - 51Lx_{hog} + 44x_{hog}^2\right) - \frac{1}{2}\left(\chi_{0,hog} - \chi_{0,sag}\right)x_{hog}\left(L - x_{hog}\right) \quad (58)$$

Where the point of contraflexure is $x_{hog}=(3/11)L$, EI_{sag} is the flexural rigidity and $\chi_{0,sag}$ is the curvature under zero moment due to shrinkage in the sagging region. Similarly, EI_{hog} is the flexural rigidity and $\chi_{0,hog}$ is the curvature under zero moment due to shrinkage in the hogging region.

From Fig. 13, it can be seen that predicted load/deflections were accurate for three of the four beams. The main contributory factors to any inaccuracy is that only two direct tension tests were performed along with the original beam tests and so any scatter in the tensile material properties is difficult to capture. Further, the shrinkage strains were not measured and here are assumed to be 500 $\mu\varepsilon$ based on later work done on the same concrete cured under the same conditions. The AFGC (2013), AS3600-2018 (Standards Australia 2018) and fib (2013) approaches were also compared where all three were found to underestimate the deflections of the continuous beams however fib (2013) was the closest to the approach suggested in this paper.

CONCLUSION

In this paper, a closed-form approach has been introduced for determining the short- and long-term deflections and crack widths in FRC and UHPFRC beams at serviceability. The advantage of this approach is that the model inputs are directly related to the results of basic material tests such as uniaxial compression, tension (or indirectly if the appropriate inverse analysis is applied), pull-out of embedded reinforcement, shrinkage and creep. Tensile stress/crack width and bond stress/slip relationships can be used in a non-linear form and as such, this approach is not semi-empirical and so does not have to be calibrated with the results of beam tests over a wide variety of beam sizes. The approach should therefore be being useful in the development of new materials, where it can be applied without the need for calibration to beam test results. These closed form solutions were validated with 12 simply supported and 4 continuous UHPFRC beams as well as 10 normal strength FRC beams where a similar level of accuracy was obtained using a range of code approaches. Some of these beams also included glass fibre reinforced polymer reinforcement demonstrating the versatility of the model. A detailed worked example is given in the supplementary material to determine the serviceability deflections and crack widths in a UHPFRC T-beam. This procedure could be used in developing design charts for use in practice for any new type of UHPFRC or FRC.

ACKNOWLEDGEMENTS

This material is based upon work supported by the Air Force Office of Scientific Research under award number FA2386-16-1-4098 and the Australian Research Council Discovery Project 190102650"

NOTATION

The following symbols are used in this paper:

A = area;

A_{c-ts} = area of tension stiffening prism;

A_{ct} = area of tensile concrete;

A_{rc}, A_{rt} = cross-sectional area of the compression and tension reinforcement, respectively;

A_0 = transformed area;

a = distance between load points under four point bending;

a_0, a_1, a_2, b_0, b_1, b_2 = coefficients to quadratic equation;

b, b_f, b_w = width of section; width of flange and width of web, respectively;

D = total depth of the section;

D_c = extension of concrete in tension stiffening prism;

d_c, d_t = depth of the compressive and tensile reinforcement, respectively;

d_f = depth of flange;

d_{NA}, $d_{NA\text{-}y}$, d_{NA0} = neutral axis depth; neutral axis depth at yield and zero moment, respectively;

$d\delta/dx$ = slip strain;

e = centroid of the total reinforcement;

E_c, E_r = elastic moduli of concrete and reinforcement, respectively

$E_{c\text{-}eff}$ = age adjusted effective elastic modulus of the concrete;

E_f = slope of the simplified tensile stress-strain relationship in Fig. 9

E_{SH} = strain hardening modulus;

EI_{cr}, EI_{uncr} = cracked and uncracked flexural rigidity, respectively;

EI_{hog}, EI_{sag} = flexural rigidity in hogging and sagging, respectively;

EI_1, EI_2 = slopes of each part of the bilinear moment-curvature relationship;

$EI_{1,hog}$, $EI_{2,hog}$ = slopes of each part of the bilinear moment-curvature relationship in hogging;

$EI_{1,sag}$, $EI_{2,sag}$ = slopes of each part of the bilinear moment-curvature relationship in sagging;

F = point load;

f_{ct} = tensile strength of concrete;

f_i, f_1, f_2, f_3 = stress intercept of stress-half crack width relationship;

f_{pc} = post-cracking strength of concrete;

f_{SH} = stress to cause microcracking;

f_y = yield stress;

I_0 = second moment of area of transformed section about the top fibre;

k = stiffness of linear ascending bond-slip relationship;

L = span of beam;

L_{def} = deformable length;

L_{per} = bonded perimeter of reinforcing bar in tension chord;

l_{ct} = lever arm of the tensile concrete;

M, M_{hy}, M_{int}, M_t, M_y, $M_{\mu cr}$ = applied moment; moment at half yield, intersection, transition point, at yield, microcracking, respectively;

M_c = moment due to concrete;

m_i, m_1, m_2, m_3 = slope of stress-half crack width relationship;

n_{FI} = modular ratio of reinforcement; E_r/E_c;

n_f = modular ratio of fibres;

P, P_c, P_{cc}, P_{ct}, P_{rc}, P_{rt} = axial force; axial force in the concrete, compressive concrete, tension concrete, compressive reinforcement and tension reinforcement, respectively;

P_{rc0}, P_{rt0} = residual load due to shrinkage and fibres in the compressive and tensile reinforcement;

S_p = primary crack spacing;

S_0 = first moment of area of transformed section about the top fibre;

w, w_{mid}, w_{sup} = crack width; crack width at midspan and support, respectively;

w_{hy}, w_t, w_y = crack width at half yield, transition and yield;

x = position in beam measured from support;

x_{hog} = distance from support to point of contraflexure;

x_1 = location of the transition moment in beam;

y = depth measured from top fibre;

α = non-linearity of non-linear ascending bond-slip relationship;

β = axial rigidity parameter;

γ = increase in stiffness due to tension stiffening;

Δ = half crack width; slip of the reinforcing bar at the crack;

Δ_i, Δ_0, Δ_1, Δ_2 = half crack width at the change in slope of half stress/crack width relationship

Δ_{mid} = midspan deflection;

δ = slip;

δ_1 = slip at maximum bond stress;

ε, ε_D, $\varepsilon_{D,t}$ = strain; strain at the bottom fibre; strain at the bottom fibre at the transition point;

ε_{ct} = effective strain in the tensile concrete;

ε_{inel} = permanent strain due to microcracking;

ε_{sh} = shrinkage strain;

ε_y = yield strain;

η = ratio of the centroid of the stress/strain relationship to the strain at the bottom fibre;

θ, θ_{sh} = rotation; rotation due to shrinkage;

λ_1, λ_2 = bond parameter for a linear ascending and non-linear bond-slip relationships, respectively;

ξ = tension stiffening parameter;

σ, σ_c, σ_{cc}, σ_{ct}, σ_{rt} = stress; stress in concrete, compressive concrete, tensile concrete and tensile reinforcement;

$\sigma_{ct\text{-}ave}$ = average tensile stress;

τ = interface shear stress; bond stress;

τ_{max} = maximum bond stress;

ϕ = creep coefficient;

χ, χ_{hy} χ_{int}, χ_t, χ_y, $\chi_{\mu cr}$, $\chi_{0,1}$ = curvature; curvature at half yield, intersection, transition, yield, microcracking, zero moment, respectively;

$\chi_{0,hog}$, $\chi_{0,sag}$ = intercept with the curvature axis in hogging or sagging, respectively;

$\chi_{0,2}$ = intercept with the curvature axis for the 1st part of the bilinear moment-curvature relationship;

$\chi_{0,1,hog}$, $\chi_{0,1,sag}$ = $\chi_{0,1}$ in hogging and sagging, respectively;

$\chi_{0,2}$ = intercept with the curvature axis for the 2nd part of the bilinear moment-curvature relationship;

$\chi_{02,hog,}$ $\chi_{02,sag}$ = $\chi_{0.2}$ in hogging and sagging, respectively;

SUPPLEMENTARY MATERIAL

The supplementary material contains a detailed worked example to demonstrate the application of the approach to determine the serviceability deflections and crack widths in a UHPFRC T-beam.

REFERENCES

AFGC (Association Francaise de Genie Civil). (2013). "Betons fibres a ultra-hautes performances- Recommandations [Ultra high performance fibre reinforced-concretes – Recommendations]." Paris, France

Amin, A., Foster, S. J., and Kaufmann, W. (2017). "Instantaneous deflection calculation for steel fibre reinforced concrete one way members." *Engineering Structures*, 131, 438-445.

Amin, A. and Gilbert, R. I. (2018). "Instantaneous Crack Width Calculation for Steel Fiber-Reinforced Concrete Flexural Members." *ACI Structural Journal*, 115(2).

Balazs, G. L. (1993). "Cracking analysis based on slip and bond stresses." *ACI Materials Journal*, 90, 340-340.

Banthia, N.,Majdzadeh, F., Wu, J., and Bindiganavile, V. (2014) "Fiber synergy in Hybrid Fiber Reinforced Concrete (HyFRC) in flexure and direct shear." *Cement and Concrete Composites*, 48, 91-97.

Barros, J. A., and Figueiras, J. A. (1999). "Flexural behavior of SFRC: testing and modeling." *ASCE J. Mater. Civ. Eng.*, 11(4), 331-339.

Barros, J. A., Taheri, M., and Salehian, H. (2015). "A model to simulate the moment–rotation and crack width of FRC members reinforced with longitudinal bars." *Engineering Structures*, 100, 43-56.

Barros, J.A., Taheri, M, and Salehian, H. (2018). "A model to predict the crack width of FRC members reinforced with longitudinal reinforcing bars." *SP-319-2*, American Concrete Institute, Farmington Hills.

Bischoff, P. H. (2003). "Tension stiffening and cracking of steel fiber-reinforced concrete." *ASCE J. Mater. Civ. Eng.*, 15(2), 174-182.

Brandt, A. M. (2008). "Fibre reinforced cement-based (FRC) composites after over 40 years of development in building and civil engineering." *Composite structures*, 86(1-3), 3-9.

Campione, G., Cucchiara, C., La Mendola, L., and Papia, M. (2005). "Steel–concrete bond in lightweight fiber reinforced concrete under monotonic and cyclic actions." *Engineering Structures*, 27(6), 881-890.

Chao, S. H., Naaman, A. E., and Parra-Montesinos, G. J. (2009). "Bond behavior of reinforcing bars in tensile strain-hardening fiber-reinforced cement composites." *ACI Structural Journal*, 106(6), 897.

Choi, C. K., and Cheung, S. H. (1996). "Tension stiffening model for planar reinforced concrete members." *Computers & Structures*, 59(1), 179-190.

Conforti, A., Minelli, F., and Plizzari, G. A. (2013). "Wide-shallow beams with and without steel fibres: a peculiar behaviour in shear and flexure." *Composites Part B: Engineering*, 51, 282-290.

Deluce, J. R., Lee, S. C., and Vecchio, F. J. (2014). "Crack model for steel fiber-reinforced concrete members containing conventional reinforcement." *ACI Structural Journal*, 111(1), 93.

Fantilli, A.P., Kwon, S., Mihashi, H. and Nishiwaki, T. (2018) “Synergy assessment in hybrid Ultra-High Performance Fiber-Reinforced Concrete (UHP-FRC).” *Cement and Concrete Composites*, 86, 19-29.

Fantilli, A.P. and Chiaia, B. (2018). “Conventional and unconventional approaches for evaluating the crack width in FRC structures.” *SP-319-4*, American Concrete Institute, Farmington Hills.

fib (International Federation for Structural Concrete). (2013). “CEB-FIP Model Code 2010.” Lausanne, Switzerland.

Gilbert, R. I., and Ranzi, G. (2010). *Time-dependent behaviour of concrete structures*. CRC Press, Boca Raton, Florida.

Graybeal, B. A. (2006). “Material property characterization of ultra-high performance concrete” *FHWA-HRT-06-103*, Federal Highways Administration, McLean, Virginia.

Gupta, A. K., and Maestrini, S. R. (1990). “Tension-stiffness model for reinforced concrete bars.” *J. Struct. Eng.*, 116(3), 769-790.

Harajli, M. H., Hout, M., and Jalkh, W. (1995). “Local bond stress-slip behavior of reinforcing bars embedded in plain and fiber concrete.” *ACI Materials Journal*, 92(4), 343-353.

Harajli, M. H. (2009). “Bond stress–slip model for steel bars in unconfined or steel, FRC, or FRP confined concrete under cyclic loading.” *J. Struct. Eng.*, 135(5), 509-518.

Hillerborg, A. (1978). “A model for fracture analysis.” *Report TVBM-3005*, Division of Building Materials, Lund Institute of Technology, Lund.

Hota, S., and Naaman, A. E. (1997). “Bond stress-slip response of reinforcing bars embedded in FRC matrices under monotonic and cyclic loading.” *ACI Structural Journal*, 94(5), 525-537.

Jungwirth, J., and Muttoni, A. (2004). “Structural behavior of tension members in Ultra High Performance Concrete.” *Proc. International Symposium on Ultra High Performance Concrete.*

Knight, D., Visintin, P., Oehlers, D. J., and Mohamed Ali, M. S. (2013). “Short-term partial-interaction behavior of RC beams with prestressed FRP and steel.” *J. Compos. Constr.*, 18(1), 04013029.

Knight, D., Visintin, P., and Oehlers, D. J. (2015). “Displacement-based simulation of time-dependent behaviour of RC beams with prestressed FRP or steel tendons.” *Structural Concrete*, 16(3), 406-417.

Lee, S. C., Cho, J. Y., and Vecchio, F. J. (2013). “Tension-Stiffening Model for Steel Fiber-Reinforced Concrete Containing Conventional Reinforcement.” *ACI Structural Journal*, 110(4).

Marchand, P., Baby, F., Khadour, A., Battesti, T., Rivillon, P., Quiertant, M., Nguyen, H.-H., Genereux, G., Deveaud, J.-P., Simon, A., and Toutlemonde, F. (2016). “Bond behaviour of reinforcing bars in UHPFRC.” *Materials and structures*, 49(5), 1979-1995.

Meda, A., Minelli, F., & Plizzari, G. A. (2012). “Flexural behaviour of RC beams in fibre reinforced concrete.” *Composites Part B: Engineering*, 43(8), 2930-2937.

Mobasher, B., Yao, Y., and Soranakom, C. (2015). “Analytical solutions for flexural design of hybrid steel fiber reinforced concrete beams.” *Engineering Structures*, 100, 164-177.

Muhamad, R., Ali, M. M., Oehlers, D. J., and Griffith, M. (2012). “The tension stiffening mechanism in reinforced concrete prisms.” *Advances in Structural Engineering*, 15(12), 2053-2069.

Ning, X., Ding, Y., Zhang, F., and Zhang, Y. (2015). “Experimental study and prediction model for flexural behavior of reinforced SCC beam containing steel fibers.” *Construction and Building Materials*, 93, 644-653.

Oesterlee, C. (2010). “Structural response of reinforced UHPFRC and RC composite members.” Ph.D. Thesis, Ecole Polytechnique Federale de Lausanne, Lausanne.

Park, S.H., Kim, D.J., Ryu, G.S. and Koh, K.T. (2012). “Tensile behavior of ultra high performance hybrid fiber reinforced concrete.” *Cement and Concrete Composites*, 34(2), 172-184.

RILEM (International Union of Laboratories and Experts in Construction Materials, Systems and Structures.) (1994) “RILEM recommendations for the testing and use of constructions materials. RC 6 bond test for reinforcement steel. 2. Pull-out test, 1983.” E & FN SPON.

Schumacher, P. (2006) “Rotation capacity of self-compacting steel fibre reinforced concrete.” PhD Thesis, Delft University, Delft.

Singh, M., Sheikh, A. H., Ali, M. M., Visintin, P., and Griffith, M. C. (2017). “Experimental and numerical study of the flexural behaviour of ultra-high performance fibre reinforced concrete beams.” *Construction and Building Materials*, 138, 12-25.

Sobuz, H. R., Visintin, P., Ali, M. M., Singh, M., Griffith, M. C., and Sheikh, A. H. (2016). “Manufacturing ultra-high performance concrete utilising conventional materials and production methods.” *Construction and Building Materials*, 111, 251-261.

Standards Australia (2009) “Concrete Structures”, *AS3600-2009*, Sydney, Australia

Standards Australia (2014). “Concrete structures-Commentary (Supplement to AS3600-2009).” *AS3600 Supplement 1:2014*, Sydney, Australia.

Standards Australia (2018) “Concrete Structures”, *AS3600-2018*, Sydney, Australia

Stang H and Aarre T (1992) “Evaluation of crack width in FRC with conventional reinforcement.” *Cement and Concrete Composites*, 14(2), 143–154.

Sturm, A.B. and Visintin, P. (2018) “Local bond slip behaviour of steel reinforcing bars embedded in UHPFRC.” *Structural Concrete,* in press.

Sturm, A.B., Visintin, P., and Oehlers, D.J. (2018a) “Mechanics of the flexural behaviour of UHPFFRC beams under instantaneous and sustained loading.” *Departmental Report, No. R 200,* School of Civil, Environmental & Mining Engineering, The University of Adelaide, Adelaide

Sturm, A.B., Visintin, P., Oehlers, D.J. and Seracino, R. (2018b) “Time dependent tension stiffening mechanics of fibre reinforced and ultra-high performance fibre reinforced concrete.” *J. Struct. Eng.*, 144(8), 04018122.

Taheri, M., Barros, J. A., & Salehian, H. (2011). “A design model for strain-softening and strain-hardening fiber reinforced elements reinforced longitudinally with steel and FRP bars.” *Composites Part B: Engineering*, 42(6), 1630-1640.

Visintin, P., Oehlers, D. J., and Haskett, M. (2013). “Partial-interaction time dependent behaviour of reinforced concrete beams.” *Engineering Structures*, 49, 408-420.

Visintin, P., and Oehlers, D. J. (2017). “Fundamental mechanics that govern the flexural behaviour of reinforced concrete beams with fibre-reinforced concrete.” *Advances in Structural Engineering*, 1369433217739705.

Visintin, P., Sturm, A.B., Mohamed Ali, M.S., and Oehlers, D.J. (2018a). “Blending macro and micro fibres to enhance to the serviceability behaviour of UHPFRC”, *Australian Journal of Civil Engineering,* in press.

Visintin, P., Ali, M., Xie, T., and Sturm, A. B. (2018b). “Experimental investigation of moment redistribution in ultra-high performance fibre reinforced concrete beams.” *Construction and Building Materials*, 166(1), 433-444.

Volkersen, O. (1938) “Die Nietkrafverteilung in zugbeanspruchten Nietverbindungen mit konstanten Laschenquerschnitten.” *Luftfahrtvorschung*, 15, 41–47.

Wille, K., El-Tawil, S., and Naaman, A. E. (2014). “Properties of strain hardening ultra high performance fiber reinforced concrete (UHP-FRC) under direct tensile loading.” *Cement and Concrete Composites*, 48, 53-66.

Wu, Z., Yoshikawa, H., and Tanabe, T. A. (1991). “Tension stiffness model for cracked reinforced concrete.” *J. Struct. Eng.*, 117(3), 715-732.

Yoo, D. Y., Shin, H. O., Yang, J. M., and Yoon, Y. S. (2014). “Material and bond properties of ultra high performance fiber reinforced concrete with micro steel fibers.” *Composites Part B: Engineering*, 58, 122-133.

Yoo, D. Y., Kwon, K. Y., Park, J. J., and Yoon, Y. S. (2015). “Local bond-slip response of GFRP rebar in ultra-high-performance fiber-reinforced concrete.” *Composite Structures*, 120, 53-64.

Yoo, D. Y., Banthia, N., and Yoon, Y. S. (2016). “Flexural behavior of ultra-high-performance fiber-reinforced concrete beams reinforced with GFRP and steel rebars.” *Engineering Structures*, 111, 246-262.

Yuguang, Y., Walraven, J. C., and den Uijl, J. A. (2009). “Combined effect of fibers and steel rebars in high performance concrete.” *Heron*, 54(2-3), 205-224.

Zhang, T., Visintin, P., and Oehlers, D. J. (2017). “Partial-interaction tension-stiffening properties for numerical simulations.” *Advances in Structural Engineering*, 20(5), 812-821.

SUPPLEMENTARY MATERIAL: DESIGN EXAMPLE

It will be shown how to determine the midspan deflection as well as the maximum crack width for the beam illustrated in Fig. S1. This procedure could be used in developing design charts for use in practice for any new type of UHPFRC or FRC.

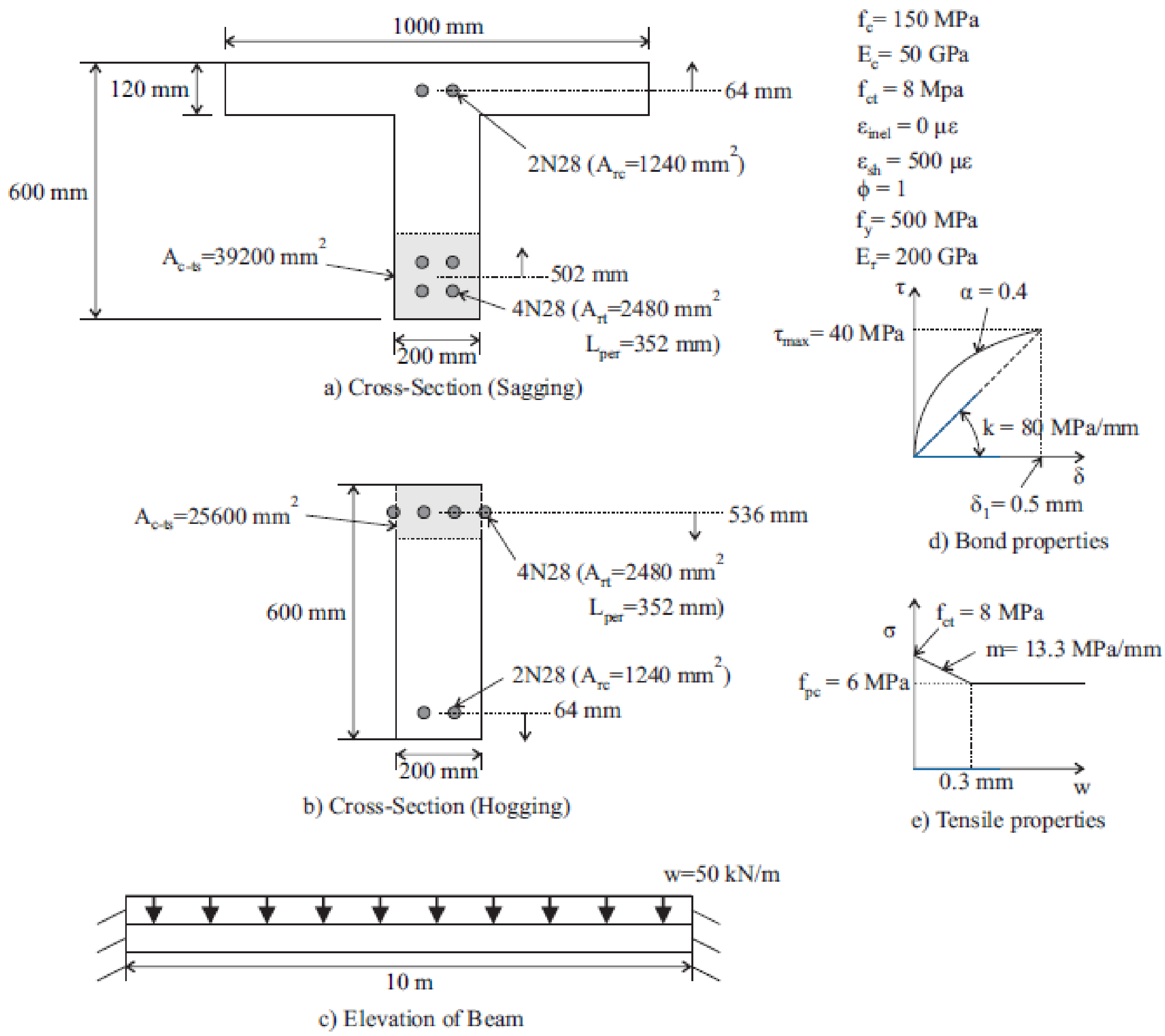

Fig. S1. Beam for design example

The effective elastic modulus of the beam allowing for the effect of creep is given by Gilbert & Ranzi (2010) as

$$E_{c-eff} = \frac{E_c}{1+\phi} = \frac{50\ GPa}{2} = 25\ GPa \qquad \text{(S1)}$$

The modular ratio n_{fi} is then given as $E_r/E_{c\text{-}eff}$=8.

To determine the deflection, first consider the sagging portion of the beam with the cross-section illustrated in Fig. S1(a).

Moment/curvature of sagging section

Crack spacing & increased stiffness due to tension stiffening

From Eq. (11)

$$\lambda_2 = \frac{(40\ MPa)(352\ mm)}{(0.5\ mm)^{0.4}}\left[\frac{1}{25000\ MPa(39200\ mm^2)} + \frac{1}{200000\ MPa(2480\ mm^2)}\right] = 56.4 \times 10^{-6} mm^{-1.4} \qquad \text{(S2)}$$

and, therefore, from Eq. (10) the crack spacing is given by

$$S_p = \left[\frac{2^{0.4}(1.4)}{(56.4\times10^{-6} mm^{-1.4})(0.6)^{1.4}}\right]^{\frac{1}{1.4}} \left[\frac{8\ MPa - 6\ MPa}{25000\ MPa}\left(\frac{25000\ MPa(39200\ mm^2)}{200000\ MPa\ (2480\ mm^2)} + 1\right)\right]^{\frac{0.6}{1.4}} = 78.4\ mm \qquad \text{(S3)}$$

From Eqs. (17), (18) and (19), the parameters for the increased stiffness due to tension stiffening are given by

$$\lambda_1 = \sqrt{80\frac{MPa}{mm}(352\ mm)\left[\frac{1}{25000\ MPa(39200\ mm^2)} + \frac{1}{200000\ MPa(2480\ mm^2)}\right]} = 0.0092\ mm^{-1} \qquad \text{(S4)}$$

$$\xi = \frac{0.0092\ mm^{-1}\frac{78.4\ mm}{2}}{\tanh\left(0.0092\ mm^{-1}\frac{78.4\ mm}{2}\right)} = 1.04 \qquad \text{(S5)}$$

$$n_f = \frac{13.3\frac{MPa}{mm}}{25000\ MPa}\frac{78.4\ mm}{2} = 0.0209 \qquad \text{(S6)}$$

Substituting Eqs. (67), (68) and (69) into Eq. (16) gives the increased stiffness due to tension stiffening as

$$\gamma = \frac{1.04 - 0.0209}{1 - 0.0209 + \frac{1.04 - 1}{\left(\frac{25000\ MPa\left(39200\ mm^2\right)}{200000\ MPa\ \left(2480\ mm^2\right)} + 1\right)}} = 1.03 \tag{S7}$$

Equivalent tensile-stress/strain relationship

The tensile-stress/crack-width relationship is converted to an equivalent stress/strain relationship by considering that the macrocrack forms at a strain of

$$\varepsilon_{D,\mu cr} = \frac{f_{SH}}{E_c} = \frac{8\ MPa}{25000\ MPa} = 320\ \mu\varepsilon \tag{S8}$$

The stress/crack-width relationship than changes slope at a crack opening of 0.3 mm. From Eq. (4), this corresponds to a strain of

$$\varepsilon_c = \frac{0.3\ \text{mm}}{78.4\ mm} + \frac{6\ MPa}{25000\ MPa} + 0 = 0.0041 \tag{S9}$$

Note that the inelastic strain due to strain hardening is zero in this design example as given in Fig. S1. This gives the effective stress/strain relationship in Fig. S2

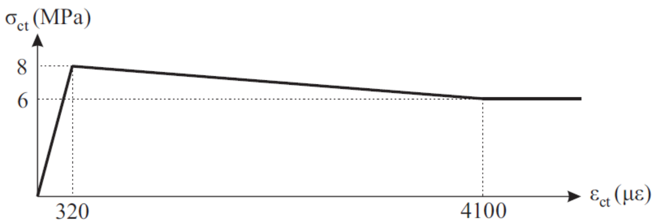

Fig. S2. Effective stress/strain relationship

Curvature under zero moment

From Eq. (42), the eccentricity parameter is given by

$$e = \frac{(2480\ mm^2)(502\ mm)+(1240\ mm^2)(64\ mm)}{2480\ mm^2+1240\ mm^2} = 356\ mm \quad \text{(S10)}$$

The transformed area of the section is given by

$$A_0 = n_{FI}A_{rt} + n_{FI}A_{rc} + (b_f - b_w)d_f + b_w D = 8(2480\ mm^2) + 8(1240\ mm^2) + (1000\ mm - 200\ mm)(120\ mm) + (200\ mm)(600\ mm) = 246 \times 10^3 mm^2 \quad \text{(A11)}$$

where b_f is the width of the flange, b_w is the width of the web and d_f is the depth of the flange.

The first moment of area about the top fibre of the transformed section is given by

$$S_0 = n_{FI}A_{rt}d_t + n_{FI}A_{rc}d_c + \frac{1}{2}(b_f - b_w)d_f^2 + \frac{1}{2}b_w D^2 = 8(2480\ mm^2)(502\ mm) + 8(1240\ mm^2)(64\ mm) + \frac{1}{2}(1000\ mm - 200\ mm)(120\ mm)^2 + \frac{1}{2}(200\ mm)(600\ mm)^2 = 52.4 \times 10^6 mm^3 \quad \text{(S12)}$$

The second moment of area about the top fibre of the transformed section is given by

$$I_0 = n_{FI}A_{rt}d_t^2 + n_{FI}A_{rc}d_c^2 + \frac{1}{3}(b_f - b_w)d_f^3 + \frac{1}{3}b_w D^3 = 8(2480\ mm^2)(502\ mm)^2 + 8(1240\ mm^2)(64\ mm)^2 + \frac{1}{3}(1000\ mm - 200\ mm)(120\ mm)^3 + \frac{1}{3}(200\ mm)(600\ mm)^3 = 19.9 \times 10^9 mm^4 \quad \text{(S13)}$$

Hence from Eq. (43), the neutral axis depth is given by

$$d_{NA0} = \frac{19.9\times10^9 mm^4 - 356\ mm(52.4\times10^6 mm^3)}{52.4\times10^6 mm^3 - 356\ mm(246\times10^3 mm^2)} = -35.4\ mm \quad \text{(S14)}$$

From Eq. (34), the curvature is then given by

$$\chi_0 = \frac{(200000\ MPa)(500\times10^{-6})(2480\ mm^2+1240\ mm^2)}{(25000\ MPa)[52.4\times10^6 mm^3+35.4\ mm(246\times10^3 mm^2)]} = 0.244 \times 10^{-6} mm^{-1} \quad \text{(S15)}$$

Moment at microcracking

Note that γ=1 before microcracking and from Eq. (15) and (22)

$$P_{rt0} = -(200000\ MPa)(2480\ mm^2)(500 \times 10^{-6}) = -248\ kN \tag{S16}$$

$$P_{rc0} = -(200000\ MPa)(2480\ mm^2)(500 \times 10^{-6}) = -124\ kN \tag{S17}$$

The average tensile concrete stress is

$$\sigma_{ct-ave} = \frac{1}{2}(25000\ MPa)(320 \times 10^{-6}) = 4\ MPa \tag{S18}$$

$$\eta = \frac{2}{3} \tag{S19}$$

To evaluate the neutral axis depth, first determine the value of the coefficients assuming that the neutral axis is in the web.

$$a_0 = E_c\varepsilon_D\left[\gamma n_{FI}A_{rt}d_t + n_{FI}A_{rc}d_c + \frac{1}{2}\left(b_f - b_w\right)d_f^2\right] + (P_{rt0} + P_{rc0})D + \sigma_{ct-ave}b_wD^2 =$$
$$(25000\ MPa)(320 \times 10^{-6})\left[8(2480\ mm^2)(502\ mm) + 8(1240\ mm^2)(64\ mm) + \right.$$
$$\left.\frac{1}{2}(1000\ mm - 200\ mm)(120\ mm)^2\right] - (248000\ N + 124000\ N)(600\ mm) +$$
$$4\ MPa(200\ mm)(600\ mm)^2 = 196 \times 10^6\ Nmm \tag{S20a}$$

$$a_1 = -E_c\varepsilon_D\left[\gamma n_{FI}A_{rt} + n_{FI}A_{rc} + \left(b_f - b_w\right)d_f\right] - (P_{rt0} + P_{rc0}) - 2\sigma_{ct-ave}b_wD =$$
$$-(25000\ MPa)(320 \times 10^{-6})[8(2480\ mm^2) + 8(1240\ mm^2) + (1000\ mm -$$
$$200\ mm)(120\ mm)] + (248000\ N + 124000\ N) - 2(4\ MPa)(200\ mm)(600\ mm) =$$
$$-1.59 \times 10^6 N \tag{S20b}$$

a_2=0 before microcracking therefore from Eq. (25) the neutral axis depth is given as

$$d_{NA,\mu cr} = \frac{196\times10^6\ Nmm}{1.59\times10^6 N} = 124\ mm \tag{S21}$$

From Eq. (23), the curvature is then given by

$$\chi_{\mu cr} = \frac{320\times10^{-6}}{600\ mm - 124\ mm} = 0.672 \times 10^{-6} mm^{-1} \tag{S22}$$

From Eq. (14), the axial force in the tensile reinforcement is given as

$$P_{rt} = 8(25000\,MPa)(2480\,mm^2)(0.672 \times 10^{-6} mm^{-1})(502\,mm - 124\,mm) - 248 \times 10^3 N = -122\,kN \quad (\,23)$$

From Eq. (21), the axial force in the compressive reinforcement is given as

$$P_{rc} = 8(25000\,MPa)(1240\,mm^2)(0.672 \times 10^{-6} mm^{-1})(64\,mm - 124\,mm) - 124 \times 10^3 N = -134\,kN \quad \text{(S24)}$$

From Eq. (2), the axial force in the tensile concrete is given as

$$P_{ct} = (4\,MPa)(200\,mm)(600\,mm - 124\,mm) = 381\,kN \quad \text{(S25)}$$

By considering that the compressive concrete behaves linear elastically, the following two components are obtained

$$P_{cc} = -0.5(1000\,mm)(124\,mm)^2(25000\,MPa)(0.672 \times 10^{-6} mm^{-1}) = -129\,kN \text{(S26)}$$

$$P_{cc2} = 0.5(1000\,mm - 200\,mm)(120\,mm - 124\,mm)^2(25000\,MPa)(0.672 \times 10^{-6} mm^{-1}) = 0.108\,kN \quad \text{(S27)}$$

Hence, the moment to cause microcracks is given as

$$M_{mcr} = -122\,kN\,(0.502\,m - 0.124\,m) - 134\,kN(0.064\,m - 0.124\,m) + 381\,kN\,\left(\frac{2}{3}\right)(0.6\,m - 0.124\,m) + 129\,kN\left(\frac{2}{3}\right)(0.124\,m) + 0.108\,kN\,\left(\frac{2}{3}\right)(0.12\,m - 0.124\,m) = 93.5\,kNm \quad \text{(S28)}$$

From Eq. (51), the uncracked flexural rigidity can be estimated as

$$EI_{uncr} = \frac{M_{mcr}}{\chi_{mcr} - \chi_0} = \frac{93.5 \times 10^6 Nmm}{(0.672 - 0.244) \times 10^{-6} mm^{-1}} = 218 \times 10^{12} Nmm^2 \quad \text{(S29)}$$

Moment at yield

From Eq. (46), the yield strain is given by

$$\varepsilon_y = \frac{1}{1.03}\left(\frac{500\ MPa}{200000\ MPa} + 500 \times 10^{-6}\right) = 0.0029 \qquad \text{(S30)}$$

To determine the neutral axis depth, assume the neutral axis is in the web, hence

$$b_0 = \left(f_y A_{rt} + P_{rc0}\right)d_t + f_1 b_w D d_t + E_c \varepsilon_y \left[n_{FI} A_{rc} d_c - \frac{1}{2} n_f b_w D^2 + \frac{1}{2}\left(b_f - b_w\right)d_f^2\right] (= [(500\ MPa)(2480\ mm^2) - 124 \times 10^3 N](502\ mm) + (8\ MPa)(200\ mm)(600\ mm)(502\ mm) + (25000\ MPa)(0.0029)\left[8(1240\ mm^2)(64\ mm) - \frac{1}{2}(0.0209)(200\ mm)(600\ mm)^2 + \frac{1}{2}(1000\ mm - 200\ mm)(120\ mm)^2\right] = 1.45 \times 10^9 mm^{-1} \qquad \text{(S31a)}$$

$$b_1 = -\left(f_y A_{rt} + P_{rc0}\right) - f_1 b_w (D + d_t) - E_c \varepsilon_y \left[n_{FI} A_{rc} - n_f b_w D + \left(b_f - b_w\right) d_f\right] = -[(500\ MPa)(2480\ mm^2) - 124 \times 10^3 N] - (8\ MPa)(200\ mm)(600\ mm + 502\ mm) - (25000\ MPa)(0.0029)[8(1240\ mm^2) - 0.0209(200\ mm)(600\ mm) + (1000\ mm - 200\ mm)(120\ mm)] = -10.5 \times 10^6 mm^{-1} \qquad \text{(S31b)}$$

$$b_2 = b_w f_1 - \frac{1}{2} b_w E_c \varepsilon_y \left(1 + n_f\right) = (200\ mm)(8\ MPa) - \frac{1}{2}(200\ mm)(25000\ MPa)(0.0029)(1 + 0.0209) = -5.80 \times 10^3 mm^{-1} \qquad \text{(S31c)}$$

Substituting in these coefficients and solving the resultant quadratic equation gives a neutral axis depth of d_{NA}=129 mm.

From Eq. (47), the resultant curvature is

$$\chi_y = \frac{0.0029}{502\ mm - 129\ mm} = 7.77 \times 10^{-6} mm^{-1} \qquad \text{(S32)}$$

The strain at the bottom fibre of the section is, therefore, given as

$$\varepsilon_{D,y} = \chi_y\left(D - d_{NA,y}\right) = (7.77 \times 10^{-6} mm^{-1})(600\ mm - 129\ mm) = 0.0037 \qquad \text{(S33)}$$

The axial force in the tensile reinforcement at yield is then

$$P_{rt} = 500\ MPa(2480\ mm^2) = 1240\ kN \tag{S34}$$

The axial force in the compressive reinforcement is given by Eq. (21)

$$P_{rc} = 200000\ MPa(1240\ mm^2)(7.77 \times 10^{-6} mm^{-1})(64\ mm - 129\ mm) - 124 \times 10^3 N = -249\ kN \tag{S35}$$

The average stress in the tensile concrete is given by Eq. (44)

$$\sigma_{ct-ave} = 8\ MPa - \frac{1}{2}(0.0209)(25000\ MPa)(0.0037) = 7.04\ MPa \tag{S36}$$

Therefore, the total axial force in the tensile concrete is given by

$$P_{ct} = 7.04\ MPa\ (200\ mm)(600\ mm - 129\ mm) = 663\ kN \tag{S37}$$

From Eq. (45),

$$\eta = \frac{\frac{1}{2}(8\ MPa) - \frac{1}{3}(0.0209)(25000\ MPa)(0.0037)}{7.04\ MPa} = 0.477 \tag{S38}$$

Hence from Eq. (5), the lever arm is given by

$$l_{ct} = 0.477(600\ mm - 129\ mm) = 225\ mm \tag{S39}$$

By considering that the compressive concrete remains linear elastic, the axial force are given as

$$P_{cc} = -\frac{1}{2}(1000\ mm)(129\ mm)^2(25000\ MPa)(7.77 \times 10^{-6} mm^{-1}) = -1620\ kN \tag{S40}$$

$$P_{cc2} = 0.5(1000\ mm - 200\ mm)(120\ mm - 129\ mm)^2(25000\ MPa)(7.77 \times 10^{-6} mm^{-1}) = 6.29\ kN \tag{S41}$$

The moment at yield is then given as

$$M_y = 1240\ kN(0.502\ m - 0.129\ m) - 249\ kN\ (0.064\ m - 0.129\ m) + 663\ kN(0.225\ m) + 1620\ kN\left(\frac{2}{3}\right)(0.129\ m) + 6.29\ kN\ \left(\frac{2}{3}\right)(0.12\ m - 0.129\ m) = 767\ kNm \qquad \text{(S42)}$$

The stress at the bottom fibre is given from the equivalent stress/strain relationship in Fig. 14 as

$$\sigma_D = 8\ MPa + (6\ MPa - 8\ MPa)\frac{0.0037-0.000320}{0.0041-0.000320} = 6.21\ MPa \qquad \text{(S43)}$$

The crack width at the bottom of the section is then given by Eq. (27) as

$$w_y = 78.4\ mm\left(0.0037 - \frac{6.21\ MPa}{25000\ MPa}\right) = 0.271\ mm \qquad \text{(S44)}$$

As this is less than 0.3 mm, the correct assumption has been made in Eq. (S7) with respect to the choice of f_i and m_i.

Moment and curvature at half yield

The strain at the bottom fibre is equal to 0.0037/2 which is 0.00185. Note that the stress at the bottom fibre is given from the equivalent stress/strain relationship as

$$\sigma_D = 8\ MPa + (6\ MPa - 8\ MPa)\frac{0.00185-0.000320}{0.0041-0.000320} = 7.19\ MPa \qquad \text{(S45)}$$

Therefore, from Eq. (3)

$$\sigma_{ct-ave} = \frac{0.5(8\ MPa)(0.000320)+0.5(8\ MPa+7.19\ MPa)(0.00185-0.00032)}{0.00185} = 6.97\ MPa \qquad \text{(S46)}$$

From Eq. (6),

$$\int_0^{\varepsilon_D} \sigma_{ct}\, \varepsilon\, d\varepsilon = 7.19\ MPa(0.00185)(0.000925) + 0.5(8\ MPa - 7.19\ MPa)(0.00185)(0.000617) = 12.7 \times 10^{-6}\ MPa \qquad \text{(S47)}$$

$$\eta = \frac{12.7\times10^{-6}\ MPa}{(0.00185)^2(6.97\ MPa)} = 0.532 \qquad \text{(S48)}$$

To determine the neutral axis depth, the following coefficients from Eq. (S2) are evaluated as

$$a_0 = E_c\varepsilon_D\left[\gamma n_{FI}A_{rt}d_t + n_{FI}A_{rc}d_c + \frac{1}{2}\left(b_f - b_w\right)d_f^2\right] + (P_{rt0} + P_{rc0})D + \sigma_{ct-ave}b_wD^2 = (25000\ MPa)(0.00185)[1.03(8)(2480\ mm^2)(502\ mm) + 8(1240\ mm^2)(64\ mm) + 0.5(1000\ mm - 200\ mm)(120\ mm)^2] - (248000\ N + 124000\ N)(600\ mm) + 6.97\ MPa(200\ mm)(600\ mm)^2 = 1.05\times10^9\ Nmm \qquad \text{(S49a)}$$

$$a_1 = -E_c\varepsilon_D\left[\gamma n_{FI}A_{rt} + n_{FI}A_{rc} + \left(b_f - b_w\right)d_f\right] - (P_{rt0} + P_{rc0}) - 2\sigma_{ct-ave}b_wD = -(25000\ MPa)(0.00185)[1.03(8)(2480\ mm^2) + 8(1240\ mm^2) + (1000\ mm - 200\ mm)(120\ mm)] + 248000\ N + 124000\ N - 2(6.97\ MPa)(200\ mm)(600\ mm) = -7.14\times10^6\ N \qquad \text{(S49b)}$$

$$a_2 = \sigma_{ct-ave}b_w - \frac{1}{2}b_wE_c\varepsilon_D = 6.97\ MPa(200\ mm) - 0.5(200\ mm)(25000\ MPa)(0.00185) = -3230\,\frac{N}{mm} \qquad \text{(S49c)}$$

The neutral axis depth is then given as 138 mm. Hence the curvature is given as

$$\chi_{hy} = \frac{0.00185}{600\ mm - 138\ mm} = 4.00\times10^{-6}mm^{-1} \qquad \text{(S50)}$$

From Eq. (14), the axial force in the tensile reinforcement is

$$P_{rt} = 1.03\ (8)(25000\ MPa)(2480\ mm^2)(4\times10^{-6}mm^{-1})(502\ mm - 138\ mm) - 248000\ N = 496\ kN \qquad \text{(S51)}$$

From Eq. (21), the axial force in the compressive reinforcement is

$$P_{rc} = 8(25000\ MPa)(1240\ mm^2)(4 \times 10^{-6}\ mm^{-1})(64\ mm - 138\ mm) - 124000\ N = -197\ kN \qquad \text{(S52)}$$

From Eq. (2), the axial force in the tensile concrete is

$$P_{ct} = 6.97\ MPa(200\ mm)(600\ mm - 138\ mm) = 644\ kN \qquad \text{(S53)}$$

By considering that the compressive reinforcement remains linear elastic

$$P_{cc} = -0.5(1000\ mm)(138\ mm)^2(25000\ MPa)(4 \times 10^{-6} mm^{-1}) = -952\ kN \qquad \text{(S54)}$$

and

$$P_{cc2} = 0.5(1000\ mm - 200\ mm)(120\ mm - 138\ mm)^2(25000\ MPa)(4 \times 10^{-6} mm^{-1}) = 13\ kN \qquad \text{(S55)}$$

From moment equilibrium,

$$M_{hy} = 496\ kN\ (0.502\ m - 0.138\ m) - 197\ kN(0.064\ m - 0.138\ m) + 644\ kN\ (0.533)(0.6\ m - 0.138\ m) + 952\ kN\ \left(\frac{2}{3}\right)(0.138\ m) + 13\ kN\ \left(\frac{2}{3}\right)(0.12\ m - 0.138\ m) = 441\ kNm \qquad \text{(S56)}$$

From Eq. (52), the cracked flexural rigidity can be estimated as

$$EI_{cr} = \frac{M_y - M_{0.5y}}{\chi_y - \chi_{0.5y}} = \frac{(767-439)\times 10^6 Nmm}{(7.77-4)\times 10^{-6} mm^{-1}} = 87.0 \times 10^{12} Nmm^2 \qquad \text{(S57)}$$

Note that the crack width at the bottom fibre is given by Eq. (27) as

$$w_{hy} = 78.4\ mm\left(0.00185 - \frac{7.19\ MPa}{25000\ MPa}\right) = 0.123 mm \qquad \text{(S58)}$$

Moment and curvature at the transition point

From Eq. (54), moment at the intersection of the cracked and uncracked curves is

$$M_{int} = \frac{\frac{767\times10^{6}Nmm}{87\times10^{12}Nmm^{2}}+0.244\times10^{-6}mm^{-1}-7.77\times10^{-6}mm^{-1}}{\frac{1}{87\times10^{12}Nmm^{2}}-\frac{1}{218\times10^{12}Nmm^{2}}} = 187kNm \quad \text{(S59)}$$

and the curvature at the intersection is given by Eq. (53) as

$$\chi_{int} = 0.244\times10^{-6}mm^{-1} + \frac{187\times10^{6}Nmm}{218\times10^{12}Nmm^{2}} = 1.10\times10^{-6}mm^{-1} \quad \text{(S60)}$$

From Eq. (55), the strain at the bottom fibre at the transition point is given by

$$\varepsilon_{D,t} = 0.00032 + [0.00185 - 0.00032]\frac{(1.10-0.672)\times10^{-6}mm^{-1}}{(4-0.672)\times10^{-6}mm^{-1}} = 517\mu\varepsilon \quad \text{(S61)}$$

Following the same procedure as for the half yield point, M_t is 172 kNm, χ_t is 1.17×10^{-6} mm^{-1} and w_t is 0.0166 mm.

Moment/curvature

Based on these calculations, the moment/curvature relationship is as shown in Fig. 15. From Eq. (29), the slope of the first part of the curve is given by

$$EI_{1,sag} = \frac{172\times10^{6}\ Nmm}{(1.17-0.244)\times10^{-6}\ mm^{-1}} = 186\times10^{12}Nmm^{2} \quad \text{(S62)}$$

and the intercept is given as $\chi_{01,sag} = 0.244\times 10^{-6}$ mm^{-1}.

The slope of the second part of the curve is given by Eq. (30) as

$$EI_{2,sag} = \frac{(767-172)\times10^{6}\ Nmm}{(7.77-1.17)\times10^{-6}\ mm^{-1}} = 90.2\times10^{12}Nmm^{2} \quad \text{(S63)}$$

and the intercept is given by Eq. (31) as

$$\chi_{02,sag} = 1.17\times10^{-6}mm^{-1} - \frac{172\times10^{6}Nmm}{90.2\times10^{12}Nmm^{2}} = -0.737\times10^{-6}mm^{-1} \quad \text{(S64)}$$

Similar calculations can be performed to determine the moment/curvature under hogging as well. The results of these calculations are illustrated in Fig. S3 where hogging is represented by the negative portion of the curve.

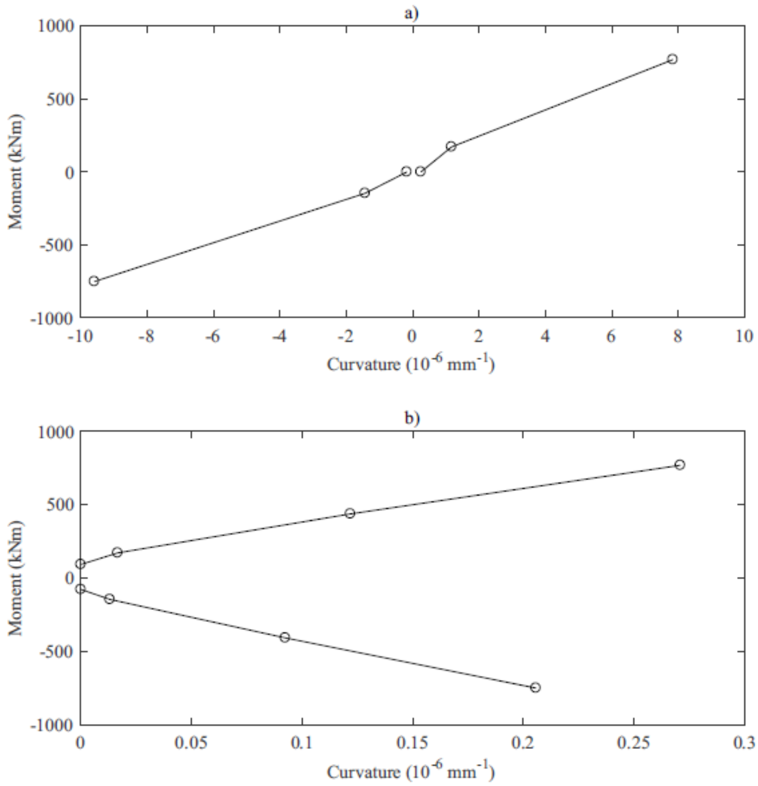

Fig. S3. Moment-curvature and moment-crack width relationships for example

For the hogging portion of the curve, the slopes are $EI_{1,hog}$=116×10^{12} $mm^{-1}$and $EI_{2,hog}$=74.2× 10^{12} mm^{-1}. The intercepts are $\chi_{01,hog}$=0.179× 10^{-6} mm^{-1} and $\chi_{02,hog}$=-0.531× 10^{-6} mm^{-1}. The cracking moment is 78 kNm, transition moment is 146 kNm, half yield moment (where half yield refers to the moment when the effective strain at the bottom fibre is half the value at yield) is 409 kNm and the yield moment is 751 kNm. The crack width at the transition point is 0.0131 mm at half yield is 0.0924 mm and at yield the crack width is 0.206 mm.

Deflections and crack widths

The midspan moment is 208 kNm and the end moment is -417 kNm which are both greater than the transition moments, hence $EI_{hog}=EI_{2,hog}$, $\chi_{0,hog}=\chi_{0,2,hog}$, $EI_{sag}=EI_{2,sag}$ and $\chi_{0,sag}=\chi_{02,sag}$. The midspan deflection of a continuous beam under a uniform distributed load is

$$\Delta_{mid} = \frac{wL^4}{384EI_{sag}} - \frac{1}{8}\chi_{0,sag}L^2 - \frac{wx_{hog}}{24}\left(\frac{1}{EI_{hog}} - \frac{1}{EI_{sag}}\right)\left(-L^3 + 4L^2x_{hog} - 6Lx_{hog}^2 + 3x_{hog}^3\right) - \frac{1}{2}\left(\chi_{0,hog} - \chi_{0,sag}\right)x_{hog}\left(L - x_{hog}\right) \quad \text{(S65)}$$

where x_{hog}=0.211L. Substituting in the values gives

$$\Delta_{mid,22} = \frac{\left(50\frac{N}{mm}\right)(10000\ mm)^4}{384(90.2\times10^{12}Nmm^2)} + \frac{1}{8}(0.737\times10^{-6}mm^{-1})(10000\ mm)^2 - \frac{\left(50\frac{N}{mm}\right)(2110\ mm)}{24}\left(\frac{1}{74.2\times10^{12}Nmm^2} - \frac{1}{90.2\times10^{12}Nmm^2}\right)[-(10000\ mm)^3 + 4(10000\ mm)^2(2110\ mm) - 6(10000\ mm)(2110\ mm)^2 + 3(2110\ mm)^3] - \frac{1}{2}(0.531 + 0.737)\times10^{-6}mm^{-1}(2110\ mm)(10000\ mm - 2110\ mm) = 17.2\ mm \quad \text{(S66)}$$

The maximum crack width at the midspan can be found as

$$w_{mid} = 0.0166\ mm + (0.123\ mm - 0.0166\ mm)\frac{208\ kNm - 172\ kNm}{441\ kNm - 172\ kNm} = 0.031\ mm \quad \text{(S67)}$$

Over the support, the maximum crack width is

$$w_{sup} = 0.0924mm\ mm + (0.206\ mm - 0.0924mm\ mm)\frac{417\ kNm - 409\ kNm}{751\ kNm - 409\ kNm} = 0.099mm \quad \text{(S68)}$$